

PREDICTION OF OPTICAL PROPAGATION LOSSES
THROUGH TURBULENT BOUNDARY/SHEAR LAYERS

A. Verhoff

McDonnell Aircraft Company
McDonnell Douglas Corporation
P.O. Box 516, St. Louis, MO 63166

SUMMARY

A simplified mathematical model has been developed which predicts the optical propagation losses which occur when an optical beam of given wave length passes through a turbulent boundary layer or shear layer. The optical losses are predicted in terms of Line Spread Function (or Strehl Ratio) and Modulation Transfer Function by using experimentally determined values of layer thickness, streamwise, lateral and beamwise density fluctuation length scales, and distribution of the standard deviation of the density fluctuations through the turbulent layer.

The prediction model has been applied to the analysis of a number of selected cases of interest from the AFWL/NASA Series II Aerodynamic-Optical Interaction wind-tunnel investigation conducted in the NASA-Ames 1.83 x 1.83 meter (6 x 6 ft) wind tunnel during July and August 1976. Direct optical measurements were available for these cases and these data have been compared with the results predicted by the aerodynamic analysis.

INTRODUCTION

Airborne optical systems are susceptible to propagation losses when the aircraft is traveling at velocities at which compressibility effects are induced in the surrounding flow field. These losses are the result of changes in index of refraction within the flow field which are directly related to variations in air density due to compressibility. Losses incurred by the optical system may be attributed to two different sources. The first consists of the propagation losses produced when the optical beam passes through the viscous boundary or shear layers which exist very near the aircraft surface. Such viscous layers are typically turbulent with randomly fluctuating air density and require a statistical analysis of the aerodynamic-optical interaction effects. The second source of optical loss is the inviscid flow field surrounding the aircraft outside its thin viscous layer within which spatial density variations are steady (or only slowly varying with time). These phenomena are sketched schematically in Figure 1.

The purpose of this investigation was to develop a simple mathematical model which predicts the optical degradation which occurs when an optical beam passes through a turbulent boundary layer or shear layer as shown in Figure 1. This model is expressed in terms of aerodynamic variables associated with the turbulent layer, such as thickness and density correlation functions and length scales.

The prediction model has been applied to the analysis of a number of selected cases of interest from the AFWL/NASA Series II Aerodynamic-Optical Interaction wind-tunnel investigation conducted in the NASA-Ames 1.83 x 1.83 meter (6 X 6 ft) wind tunnel during July and August 1976. Direct optical measurements were available for these cases and these data have been compared with the results predicted by the aerodynamic analysis.

SYMBOL LIST

A	-	wave amplitude
B	-	function in Optical Transfer Function relation
D	-	aperture diameter
F	-	function proportional to error integral
G	-	pupil function
K	-	Gladstone-Dale constant
P	-	optical power
Q	-	function in Optical Transfer Function relation
R	-	density correlation function
S	-	Line Spread Function
T	-	averaging time
X	-	spatial frequency
a	-	longitudinal (streamwise) correlation length scale
b	-	lateral correlation length scale
c	-	normal (beamwise) correlation length scale
d	-	correlation function parameter $\sqrt{\left(\frac{x}{a}\right)^2 + \left(\frac{y}{b}\right)^2}$
e	-	exponential function
f	-	function in Optical Transfer Function relation
g	-	function in Optical Transfer Function relation
h	-	function in Optical Transfer Function relation
i	-	complex number ($\sqrt{-1}$)
k	-	wave number
r	-	radial coordinate $\sqrt{x^2 + y^2}$
t	-	time
u	-	argument of Optical Transfer Function
x	-	spatial coordinate (streamwise)
y	-	spatial coordinate (lateral)
z	-	spatial coordinate (beamwise)
α	-	approximation parameter
β	-	approximation parameter
δ	-	boundary/shear layer thickness
ζ	-	spatial coordinate (beamwise)
η	-	spatial coordinate (lateral)
λ	-	wave length

ξ	-	spatial coordinate (streamwise)
ρ	-	mass density
σ	-	density fluctuation scale factor
τ	-	Optical Transfer Function
Δ	-	wave phase
Σ	-	aperture area
Δ_m	-	mean component of wave phase
Δ_r	-	random component of wave phase
G_m	-	mean component of pupil function
ϕ_{12}	-	covariance function of wave phase fluctuations
σ_1	-	standard deviation of wave phase fluctuations
σ_2	-	standard deviation of wave phase fluctuations
ρ_m	-	mean component of mass density
ρ_r	-	random component of mass density
ρ_r'	-	standard deviation of density fluctuations
$\bar{\tau}$	-	time-averaged Optical Transfer Function
τ_o	-	diffraction limited Optical Transfer Function
\bar{x}	-	normalized spatial frequency
\bar{y}	-	normalized spatial frequency
\bar{r}	-	normalized spatial frequency
S_L	-	Line Spread Strehl Ratio
\dot{m}	-	mass injection rate
M_∞	-	free stream Mach number
Re	-	Reynolds number per meter

ANALYSIS

Optical propagation losses through a flow field of varying index of refraction may be quantified by means of the Optical Transfer Function. This function is defined as the normalized two-dimensional Fourier transform of the focal plane image of a point source. The Optical Transfer Function may also be expressed directly as a function of the optical wave in the aperture plane. That is,

$$\tau(\bar{x}, \bar{y}, t) = \frac{1}{P} \iint_{-\infty}^{\infty} G^*(\xi, \eta, t) G(\xi+x, \eta+y, t) d\xi d\eta$$

where the pupil function G is defined as

$$G(\xi, \eta, t) = \begin{cases} A(\xi, \eta, t) e^{ik\Delta(\xi, \eta, t)}; & (\xi, \eta) \in \Sigma \\ 0 & ; (\xi, \eta) \notin \Sigma \end{cases}$$

and the optical power is

$$P = \iint_{-\infty}^{\infty} G^*(\xi, \eta, t) G(\xi, \eta, t) d\xi d\eta$$

The wave amplitude and phase are denoted by A and Δ while k is the wave number and Σ is the aperture area. Spatial coordinates in the aperture plane are (x, y) and (ξ, η) and an asterisk (*) denotes complex conjugate. Normalized spatial frequencies in the focal plane are \bar{x} and \bar{y} . Since the turbulent flow through which the optical beam passes is random, both the amplitude and phase are dependent on the time t .

According to Tatarski (Reference 1) random amplitude effects can be considered negligible compared to random phase effects for the wave lengths λ and viscous layer thicknesses being considered in this analysis. Therefore, the above relations may be simplified to

$$G(\xi, \eta, t) = \begin{cases} A(\xi, \eta) e^{ik\Delta(\xi, \eta, t)}; & (\xi, \eta) \in \Sigma \\ 0 & ; (\xi, \eta) \notin \Sigma \end{cases}$$

and

$$P = \iint_{-\infty}^{\infty} [A(\xi, \eta)]^2 d\xi d\eta$$

As normally done in turbulent flow analyses, the pupil function G and phase Δ may be decomposed into mean and random components. That is,

$$\Delta(\xi, \eta, t) = \Delta_m(\xi, \eta) + \Delta_r(\xi, \eta, t) \quad (1)$$

and

$$G_m(\xi, \eta) = \begin{cases} A(\xi, \eta) e^{ik\Delta_m(\xi, \eta)} & ; (\xi, \eta) \in \Sigma \\ 0 & ; (\xi, \eta) \notin \Sigma \end{cases} \quad (2)$$

The Optical Transfer Function then becomes

$$\tau(\bar{x}, \bar{y}, t) = \frac{1}{P} \iint_{-\infty}^{\infty} G_m^*(\xi, \eta) G_m(\xi+x, \eta+y) e^{ik[\Delta_r(\xi+x, \eta+y, t) - \Delta_r(\xi, \eta, t)]} d\xi d\eta \quad (3)$$

Assuming a Gaussian joint probability density function for the random quantities $\Delta_r(\xi+x, \eta+y, t)$ and $\Delta_r(\xi, \eta, t)$, the expected value of τ may be written (Reference 2)

$$\langle \tau(\bar{x}, \bar{y}, t) \rangle = \frac{1}{P} \iint_{-\infty}^{\infty} G_m^*(\xi, \eta) G_m(\xi+x, \eta+y) e^{-k^2 [\frac{1}{2}(\sigma_1^2 + \sigma_2^2) - \phi_{12}]} d\xi d\eta \quad (4)$$

where

$$\sigma_1^2 \equiv \langle \Delta_r(\xi+x, \eta+y, t)^2 \rangle \quad (5)$$

$$\sigma_2^2 \equiv \langle \Delta_r(\xi, \eta, t)^2 \rangle \quad (6)$$

and

$$\phi_{12} \equiv \langle \Delta_r(\xi+x, \eta+y, t) \Delta_r(\xi, \eta, t) \rangle \quad (7)$$

This assumption is equivalent to approximating the quantity

$$e^{ik[\Delta_r(\xi+x, \eta+y, t) - \Delta_r(\xi, \eta, t)]}$$

in Equation (3) by the first and second moments of $\Delta_r(\xi+x, \eta+y, t)$ and $\Delta_r(\xi, \eta, t)$.

For steady mean flow conditions, the expected values of the above quantities in Equations (5), (6) and (7) may be replaced by time averages. That is,

$$\sigma_1^2 = \frac{1}{T} \int_0^T [\Delta_r(\xi+x, \eta+y, t)]^2 dt \quad (8)$$

$$\sigma_2^2 = \frac{1}{T} \int_0^T [\Delta_r(\xi, \eta, t)]^2 dt \quad (9)$$

and

$$\phi_{12} = \frac{1}{T} \int_0^T \Delta_r(\xi, \eta, t) \Delta_r(\xi+x, \eta+y, t) dt \quad (10)$$

The instantaneous wave phase may be expressed in terms of the instantaneous density according to

$$\Delta(x, y, t) = K \int_0^\delta \rho(x, y, z, t) dz$$

where K is the Gladstone-Dale constant and δ denotes the turbulent boundary/shear layer thickness. In terms of mean and random density components

$$\Delta_m(x, y) = K \int_0^\delta \rho_m(x, y, z) dz \quad (11)$$

and

$$\Delta_r(x, y, t) = K \int_0^\delta \rho_r(x, y, z, t) dz \quad (12)$$

Using Equation (12) in Equation (10),

$$\phi_{12} = \frac{K^2}{T} \int_0^T \int_0^\delta \rho_r(\xi, \eta, \zeta, t) d\zeta \int_0^\delta \rho_r(\xi+x, \eta+y, \zeta', t) d\zeta' dt$$

Since ζ and ζ' are independent

$$\phi_{12} = \frac{K^2}{T} \int_0^T \int_0^\delta \int_0^\delta \rho_r(\xi, \eta, \zeta, t) \rho_r(\xi+x, \eta+y, \zeta', t) d\zeta' d\zeta dt$$

With the substitution $z = \zeta' - \zeta$, this expression becomes (after interchanging the time and spatial order of integration)

$$\phi_{12} = \frac{K^2}{T} \int_0^\delta \int_{-\zeta}^{\delta-\zeta} \int_0^T \rho_r(\xi, \eta, \zeta, t) \rho_r(\xi+x, \eta+y, \zeta+z, t) dt dz d\zeta \quad (13)$$

In a like manner, Equations (8) and (9) may be written

$$\sigma_1^2 = \frac{K^2}{T} \int_0^\delta \int_{-\zeta}^{\delta-\zeta} \int_0^T \rho_r(\xi+x, \eta+y, \zeta, t) \rho_r(\xi+x, \eta+y, \zeta+z, t) dt dz d\zeta \quad (14)$$

$$\sigma_2^2 = \frac{K^2}{T} \int_0^\delta \int_{-\zeta}^{\delta-\zeta} \int_0^T \rho_r(\xi, \eta, \zeta, t) \rho_r(\xi, \eta, \zeta+z, t) dt dz d\zeta \quad (15)$$

The time integrations in each of these expressions may be related to the density correlation function R and standard deviation of the random density fluctuations ρ_r' . That is,

$$\frac{1}{T} \int_0^T \rho_r(\xi, \eta, \zeta, t) \rho_r(\xi+x, \eta+y, \zeta+z, t) dt = [\rho_r'(\xi, \eta, \zeta)]^2 R(\xi, \eta, \zeta; x, y, z) \quad (16)$$

$$\frac{1}{T} \int_0^T \rho_r(\xi+x, \eta+y, \zeta, t) \rho_r(\xi+x, \eta+y, \zeta+z, t) dt = [\rho_r'(\xi+x, \eta+y, \zeta+z)]^2 R(\xi+x, \eta+y, \zeta+z; 0, 0, -z) \quad (17)$$

$$\frac{1}{T} \int_0^T \rho_r(\xi, \eta, \zeta, t) \rho_r(\xi, \eta, \zeta+z, t) dt = [\rho_r'(\xi, \eta, \zeta)]^2 R(\xi, \eta, \zeta; 0, 0, z) \quad (18)$$

Making use of the above results, the expected value or time-averaged value of the Optical Transfer Function (denoted now by $\bar{\tau}$) expressed in Equation (4) becomes

$$\overline{\tau(\bar{x}, \bar{y})} = \frac{1}{P} \int_{-\infty}^{\infty} \int_{-\infty}^{\infty} G_m^*(\xi, \eta) G_m(\xi+x, \eta+y) \exp \left\{ -K^2 k^2 \delta^2 \int_0^1 \int_{-\zeta}^{1-\zeta} \right. \\ \left. \left[\frac{1}{2} \rho_r'(\xi, \eta, \zeta)^2 R(\xi, \eta, \zeta; 0, 0, z) + \frac{1}{2} \rho_r'(\xi+x, \eta+y, \zeta+z)^2 \right. \right. \\ \left. \left. R(\xi+x, \eta+y, \zeta+z; 0, 0, -z) - \rho_r'(\xi, \eta, \zeta)^2 R(\xi, \eta, \zeta; x, y, z) \right] dz d\zeta \right\} d\xi d\eta \quad (19)$$

In this relationship, spatial coordinates have been normalized by the boundary/shear layer thickness δ .

For the experimental conditions described in the next section, the following assumptions can be made:

- o Flow is two-dimensional (no η dependence of mean flow properties or turbulence intensity and correlation functions)
- o Variations of mean flow properties and turbulence quantities in the longitudinal flow direction (ξ) are negligible compared to those in the normal beamwise direction (ζ)
- o Wave amplitude A is uniform in the aperture plane
- o Density correlation functions may be approximated by

$$e^{-\sqrt{\left(\frac{x}{a}\right)^2 + \left(\frac{y}{b}\right)^2 + \left(\frac{z}{c}\right)^2}}$$

where a , b and c denote correlation length scales in terms of boundary/shear layer thickness

- o For given flow conditions, length scales a , b and c are constant

The exponential approximation for the density correlation function was chosen because it more nearly approximates the shape of experimentally measured results than, for instance, a Gaussian shape (Reference 3) while still providing a high degree of mathematical simplicity.

With the above approximations Equation (19) may be simplified to

$$\overline{\tau(\bar{x}, \bar{y})} = \tau_o(\bar{r}) \exp \left\{ -\frac{1}{2} K^2 k^2 \delta^2 \int_0^1 \int_{-\zeta}^{1-\zeta} [\rho_r'(\zeta)^2 + \rho_r'(\zeta+z)^2] e^{-\left|\frac{z}{c}\right|} dz d\zeta \right. \\ \left. + K^2 k^2 \delta^2 \int_0^1 \rho_r'(\zeta)^2 \int_{-\zeta}^{1-\zeta} e^{-\sqrt{\left(\frac{x}{a}\right)^2 + \left(\frac{y}{b}\right)^2 + \left(\frac{z}{c}\right)^2}} dz d\zeta \right\} \quad (20)$$

where τ_o is the diffraction limited Optical Transfer Function. For a circular aperture of diameter D

$$\tau_o(\bar{r}) = \begin{cases} \frac{2}{\pi} \left[\cos^{-1} \left(\frac{r\delta}{D} \right) - \left(\frac{r\delta}{D} \right) \sqrt{1 - \left(\frac{r\delta}{D} \right)^2} \right]; & 0 \leq r \leq D/\delta \\ 0 & ; r > D/\delta \end{cases}$$

where r is the radial location $\sqrt{x^2 + y^2}$ (normalized by δ) and \bar{r} is the normalized spatial frequency.

In order to further simplify this analysis, the integrand $e^{-\sqrt{d^2 + \left(\frac{z}{c}\right)^2}}$ in Equation (20) where

$$d = \sqrt{\left(\frac{x}{a}\right)^2 + \left(\frac{y}{b}\right)^2}$$

will be approximated by $e^{-d} e^{-\alpha^2 \left(\frac{z}{c}\right)^2 - \beta \left(\frac{z}{c}\right)}$. Both functions have the same value at $z = 0$ while the parameters α and β may be determined such that the approximation coincides with the integrand in value and slope at the value of z for half amplitude. That is,

$$\alpha^2 = [d^2 + \ln 2 (\ln 2 + 2d)]^{-1/2} - [\ln 2 + 2d]^{-1}$$

and

$$\beta = \ln 2 [\ln 2 (\ln 2 + 2d)]^{-1/2} - \alpha^2 [\ln 2 (\ln 2 + 2d)]^{1/2}$$

The accuracy of this approximation is shown in Figure 2 for several values of d. With this simplification, the inner integrations in Equation (20) may be carried out with the result

$$\begin{aligned} \overline{\tau(x, y)} = \tau_o(\bar{r}) \exp \left\{ -K^2 k^2 \delta^2 c \int_0^1 \rho_r'(\zeta)^2 \left(2 - e^{-\frac{\zeta}{c}} - e^{\frac{\zeta-1}{c}} \right) d\zeta + \right. \\ \left. K^2 k^2 \delta^2 \frac{c}{\alpha} e^{\frac{1}{4} \left(\frac{\beta}{\alpha}\right)^2 - d} \int_0^1 \rho_r'(\zeta)^2 \left[F\left(\frac{\alpha\zeta}{c} + \frac{1}{2} \frac{\beta}{\alpha}\right) + \right. \right. \\ \left. \left. F\left(\frac{\alpha}{c} - \frac{\alpha\zeta}{c} + \frac{1}{2} \frac{\beta}{\alpha}\right) - 2F\left(\frac{1}{2} \frac{\beta}{\alpha}\right) \right] d\zeta \right\} \end{aligned} \quad (21)$$

where F is proportional to the error function integral (Reference 4) and is defined as

$$F(z) = \int_0^z e^{-t^2} dt$$

A final simplification will be made with the assumption

$$\rho'_r(\zeta) = 4\sigma\zeta(1-\zeta) \quad (22)$$

where σ is a scale factor dependent on the flow conditions. This approximation does not destroy any fundamental variable dependency and any numerical error introduced after the integrations in Equation (21) are carried out should be within the experimental errors associated with the various fluid dynamic parameters. Specifically, the integrals in Equation (21) become

$$\int_0^1 \rho'_r(\zeta)^2 \left(2 - e^{-\zeta/c} - e^{-\frac{\zeta-1}{c}} \right) d\zeta = 16\sigma^2 \left[\frac{1}{15} - 4c^3(12c^2 - 6c + 1) + 4c^3(12c^2 + 6c + 1) e^{-1/c} \right]$$

and

$$\int_0^1 \rho'_r(\zeta)^2 \left[F\left(\frac{\alpha\zeta}{c} + \frac{1}{2} \frac{\beta}{\alpha}\right) + F\left(\frac{\alpha}{c} - \frac{\alpha\zeta}{c} + \frac{1}{2} \frac{\beta}{\alpha}\right) - 2F\left(\frac{1}{2} \frac{\beta}{\alpha}\right) \right] d\zeta =$$

$$\sigma^2 \left\{ f \left(\frac{c}{\alpha}\right)^2 e^{-\left(\frac{\alpha}{c} + \frac{1}{2} \frac{\beta}{\alpha}\right)^2} - g \left(\frac{c}{\alpha}\right)^4 e^{-\frac{1}{4} \left(\frac{\beta}{\alpha}\right)^2} + \left[\frac{16}{15} + h \left(\frac{c}{\alpha}\right)^5 \right] \left[F\left(\frac{\alpha}{c} + \frac{1}{2} \frac{\beta}{\alpha}\right) - F\left(\frac{1}{2} \frac{\beta}{\alpha}\right) \right] \right\}$$

where

$$f = \frac{8}{15} - \frac{4}{15} \left(1 + \frac{\beta}{c}\right) \left(\frac{c}{\alpha}\right)^2 + 4 \left[\frac{8}{5} + \frac{11}{10} \left(\frac{\beta}{c}\right)^2 + \frac{1}{30} \left(\frac{\beta}{c}\right)^2 \right] \left(\frac{c}{\alpha}\right)^4 + 2 \left(\frac{\beta}{c}\right)^2 \left(\frac{9}{5} + \frac{3}{10} \frac{\beta}{c}\right) \left(\frac{c}{\alpha}\right)^6 + \frac{1}{5} \left(\frac{\beta}{c}\right)^4 \left(\frac{c}{\alpha}\right)^8$$

$$g = \frac{16}{3} + 8 \left[\frac{4}{5} + \frac{5}{4} \frac{\beta}{c} + \frac{1}{6} \left(\frac{\beta}{c}\right)^2 \right] \left(\frac{c}{\alpha}\right)^2 + 2 \left(\frac{\beta}{c}\right)^2 \left(\frac{9}{5} + \frac{1}{2} \frac{\beta}{c}\right) \left(\frac{c}{\alpha}\right)^4 + \frac{1}{5} \left(\frac{\beta}{c}\right)^4 \left(\frac{c}{\alpha}\right)^6$$

and

$$h = 12 + 8 \frac{\beta}{c} + 12 \frac{\beta}{c} \left[1 + \frac{\beta}{c} + \frac{1}{9} \left(\frac{\beta}{c} \right)^2 \right] \left(\frac{c}{\alpha} \right)^2 + 4 \left(\frac{\beta}{c} \right)^3 \left(1 + \frac{1}{4} \frac{\beta}{c} \right) \left(\frac{c}{\alpha} \right)^4 + \frac{1}{5} \left(\frac{\beta}{c} \right)^5 \left(\frac{c}{\alpha} \right)^6$$

Defining

$$B = \frac{16}{15} c - 64c^4 \left[12c^2 - 6c + 1 + (12c^2 + 6c + 1) e^{-1/c} \right]$$

and

$$Q = g \left(\frac{c}{\alpha} \right)^5 - f \left(\frac{c}{\alpha} \right)^3 e^{-\left(\frac{c}{\alpha} \right)^2 - \frac{\beta}{c} - \frac{c}{\alpha} \left[\frac{16}{15} + h \left(\frac{c}{\alpha} \right)^5 \right] \left[F \left(\frac{\alpha}{c} + \frac{1}{2} \frac{\beta}{\alpha} \right) - F \left(\frac{1}{2} \frac{\beta}{\alpha} \right) \right] e^{\frac{1}{4} \left(\frac{\beta}{\alpha} \right)^2}$$

then Equation (21) for the time-averaged Optical Transfer Function becomes

$$\overline{\tau(\bar{x}, \bar{y})} = \tau_o(\bar{r}) \exp \left\{ -K^2 k^2 \delta^2 \sigma^2 \left[B + Q e^{-d} \right] \right\} \quad (23)$$

where

$$d = \sqrt{\left(\frac{x}{a} \right)^2 + \left(\frac{y}{b} \right)^2}$$

Because $\bar{\tau}$ in Equation (23) is real and non-negative due to the assumptions underlying its derivation, $\bar{\tau}$ is identical to the Modulation Transfer Function. Another quantity useful in describing optical system performance is the Line Spread Function S, which is the one-dimensional Fourier Transform of the Optical Transfer Function. Considering only the case $y = 0$, $\bar{\tau}$ becomes an even function of x and, after normalization,

$$S(X) = \frac{3\pi}{4} \int_0^1 \cos(2\pi Xu) \bar{\tau}(u) du \quad (24)$$

where X represents spatial frequency and

$$\bar{\tau}(u) = \frac{2}{\pi} \left[\cos^{-1}u - u \sqrt{1-u^2} \right] \exp \left\{ -K^2 k^2 \delta^2 \sigma^2 \left[B + Q e^{-\frac{D}{\delta a} u} \right] \right\} \quad (25)$$

where

$$u = \frac{x\delta}{D} \quad (26)$$

The peak value of S (i.e., $X = 0$) is defined as the Line Spread Strehl Ratio S_L and depends only on the optical beam wave length and diameter and the fluid dynamic properties of the turbulent flow.

APPLICATION OF MATHEMATICAL PREDICTION MODEL TO EXPERIMENTAL TEST RESULTS

The effect of random density fluctuations on the propagation of an optical beam through a turbulent boundary or shear layer is described in general by Equation (19) in terms of density correlation functions and standard deviations. The test conditions existing during the AFWL Series II Aero-Optical wind-tunnel investigation in the NASA Ames 1.83 x 1.83 meter (6 x 6 ft) tunnel allow a number of simplifying assumptions resulting in the aerodynamic-optical interaction relationship given by Equation (25). A complete description of the aerodynamic test conditions, basic instrumentation and mean flow properties within the turbulent boundary/shear layer is given in Reference 5.

Both aerodynamic and optical data were obtained from the flat plate-cavity model shown schematically in Figure 3. The cavity was cubical in shape and measured 15.2 cm per side. The turbulent boundary layer which developed on the plate could be artificially thickened by either a set of pins (called V-K pins) or porous fences. Both devices were removable allowing for a clean plate configuration. The cavity was equipped with a bottom window and could also be covered by a flush window if desired.

Hot wire sensors were mounted on a movable probe which could be traversed in the normal (z) direction and on a stationary probe which could be fixed at several different normal locations. This arrangement allowed the measurement by NASA experimenters of fluctuation intensities and correlation functions within the turbulent layer. The hot wire sensors could also be inserted through the cavity walls for measurement within the cavity itself. Velocity fluctuation intensities and correlation functions were also measured independently in the turbulent layer and within the cavity by means of a Laser-Doppler Velocimeter shown in Figure 3. Optical measurements were obtained by AFWL experimenters by passing a He-Ne laser beam ($\lambda = .6328 \times 10^{-6}$ meters) through the cavity window(s) and reflecting it back through the cavity from the return mirror mounted in the free stream tunnel flow. The optical measurement equipment is not shown in Figure 3.

A summary of the many possible geometrical configurations which could be achieved by the wind-tunnel model is presented in Table 1. Nearly all of the configurations were tested at nominal free stream Mach numbers of 0.6, 0.7, 0.8 and 0.9 and nominal free stream Reynolds numbers of 6.6×10^6 and 9.8×10^6 per meter. Because the optical measurements could not be made simultaneously with the aerodynamic measurements because of instrumentation space limitations, each configuration was tested twice.

Five different configurations at nominal free stream Mach numbers of 0.6 and 0.9 and nominal free stream Reynolds number of 9.8×10^6 per meter were selected as being of particular interest. These configurations are denoted in the matrix in Table 1 by the AFWL designated configuration number. The mathematical prediction model was used to analyze these configurations. Aerodynamic data for these configurations were supplied by NASA (Reference 6) and are summarized in subsequent figures while the optical data were supplied by AFWL (Reference 7). A discussion of the mathematically predicted results using the aerodynamic data and the comparison of these results with direct optical measurements is presented below. The predicted results assume a perfectly correlated double pass from the return mirror through the turbulent layer.

Configuration #1

This configuration consisted of the flat plate with cavity covered and the V-K pins upstream to artificially thicken the turbulent boundary layer as sketched in Figure 4. The turbulent boundary-layer thickness showed little change with Mach number since for the most part the thickness is artificially induced by the V-K pins. The density fluctuation intensity level, however, does show an increase with Mach number.

Predicted Line Spread Strehl Ratios computed from Equation (24) using the aerodynamic data are shown in Figure 5. Optical measurements at several beam diameters are also shown for comparison and the agreement is reasonably good. Modulation Transfer Functions for several beam diameters were also predicted from the aerodynamic data using Equation (25). These results are shown in Figures 6, 7, and 8 along with direct optical measurements of the Modulation Transfer Function. The aerodynamic predictions show the expected decrease in optical beam quality with increasing Mach number and beam diameter while the optical measurements show the opposite trend with Mach number at the larger beam diameters. Line Spread Functions were computed from the optically measured Modulation Transfer Functions for this configuration using Equation (24) and compared with those predicted from the aerodynamic data. These results are shown in Figures 9, 10, and 11.

Configuration #8

This configuration consisted of the clean plate with the cavity open as sketched in Figure 12. A normal turbulent boundary layer developed along the plate which separated as a turbulent shear layer over the open cavity. The shear layer showed a significant increase in thickness and fluctuation intensity with Mach number as expected.

Line Spread Strehl Ratios predicted from the aerodynamic data are shown in Figure 13; direct optical measurements of Strehl Ratio for this configuration were not available. According to these results, the open cavity shear layer was better optically at the lower Mach number and worse at the higher Mach number than the thickened turbulent boundary-layer results shown in Figure 5. Modulation Transfer Functions for two beam diameters were predicted from the aerodynamic data and are compared with direct optical measurements in Figures 14 and 15. Both the aerodynamic predictions and optical measurements show the expected decrease in optical beam quality with increase in Mach number and beam diameter although they do not agree closely with each other.

Configuration #11

This configuration consisted of the plate with cavity open and a fence (4.6 cm height, 38% porosity) mounted upstream of the cavity as sketched in Figure 16. The cavity-fence arrangement produced a thinner turbulent shear layer over the open cavity than the clean plate with open cavity arrangement of Configuration #8. However, larger fluctuation intensities were induced by the fence. Both the shear layer thickness and fluctuation intensity increased substantially with Mach number.

Line Spread Strehl Ratios predicted from the aerodynamic data are shown in Figure 17; direct optical measurements for comparison were not available. Comparison of these results with those of Figure 13 show that the fence produced a higher level of optical degradation than the clean plate configuration. Modulation Transfer Functions for two beam diameters were predicted from the aerodynamic measurements and are compared with optical measurements in Figures 18 and 19. Although their agreement is not good, both the aerodynamically predicted results and optical measurements show the proper trend with beam diameter and Mach number.

Configuration #13

This configuration also consisted of the plate with cavity open and a fence (2.3 cm height, 58% porosity) mounted upstream of the cavity as sketched in Figure 20. This fence produced a thicker shear layer over the open cavity than the fence of Configuration #11 with about the same level of fluctuation intensity. Both the shear layer thickness and fluctuation intensity increased significantly with Mach number.

Line Spread Strehl Ratios predicted from the aerodynamic data are shown in Figure 21. Optical measurements of Strehl Ratio for several beam diameters are also shown for comparison. Agreement between the two is poor with the optical measurements showing improved performance with increasing beam diameter in contrast to the aerodynamic predictions. Based upon the aerodynamic prediction, the shorter fence of this configuration produced less optical degradation at low Mach numbers and more at high Mach numbers than the taller fence of Configuration #11. Modulation Transfer Functions for several beam diameters as predicted from the aerodynamic data are presented in Figures 22, 23 and 24 along with direct optical measurements for comparison. Both data sets show decreasing optical quality with increase in beam diameter and Mach number although only a weak Mach number dependence is evident from the optical measurements.

Configuration #14

This configuration consisted of the clean plate with cavity open and a porous cavity front wall for mass injection into the cavity as sketched in Figures 25 and 29. For the case of zero mass injection (Figure 25), the porous front wall acted as an acoustic damper and decreased the turbulent shear layer thickness over the cavity by a slight amount but caused an increase in fluctuation intensity as can be seen by referring to Figure 12. A nominal mass injection rate of .25 kg/sec (Figure 29) had little or no effect on the shear layer thickness or fluctuation intensity, although in either case both quantities increased significantly with Mach number.

Line Spread Strehl Ratios for the case of zero mass injection predicted from the aerodynamic measurements are shown in Figure 26 along with optically measured values for several beam diameters. Agreement is again poor with the optical measurements showing little change in degradation level with beam diameter. Based upon the aerodynamic predictions, the porous cavity front

wall caused some increase in optical degradation as can be seen from Figure 13 which corresponds to the case with solid cavity front wall. Results with mass injection shown in Figure 30 show some increase in beam quality over the zero mass injection case of Figure 26 with degradation levels approximately the same as the solid front wall case of Figure 13.

Modulation Transfer Functions for two beam diameters were predicted from the aerodynamic measurements and are compared with direct optical measurements in Figures 27 and 28 for the case of zero mass injection and Figures 31 and 32 for the mass injection case. Although their agreement is not close, both sets of measurements exhibit increasing optical degradation with increase in beam diameter and Mach number.

CONCLUSIONS

Qualitatively, the predictions based on the aerodynamic data consistently show for all of the cases analyzed the correct trend of increasing optical degradation with increase in Mach number (i.e., compressibility effect) and increase in beam diameter. However, for some of the cases the optical measurements show the opposite trends. Analysis of static pressure data has shown (Reference 5) that the return mirror mount located within the tunnel flow induced substantial longitudinal and beamwise pressure (and density) gradients in the tunnel flow between the return mirror and flat plate model. Such gradients undoubtedly have a detrimental effect on optical propagation through this region thereby adversely affecting the optical measurements. Other factors such as mechanical vibration of the optical instrumentation or flow induced vibration of the return mirror also affect the optical measurements and contribute to the differences between the measured and predicted results.

Quantitatively, the aerodynamic predictions and the optical measurements of Strehl Ratio show reasonably good agreement for the flat plate with thickened turbulent boundary layer (Configuration #1). However, the agreement is poor for the other two cases for which Strehl Ratio data were available, namely the open cavity with short boundary-layer fence (Configuration #13) and the open cavity with porous front wall and zero mass injection (Configuration #14). The Modulation Transfer Function comparisons show reasonably good agreement for only a few of the cases and primarily at the smallest beam diameters tested. In general, the optically measured Modulation Transfer Functions show considerably higher levels of optical degradation than those predicted from the aerodynamic measurements. Based upon the aerodynamic predictions, the most optically favorable configuration of those analyzed appears to be the clean plate with cavity open and mass injection (Configuration #14).

Because of the desirability of using a predictive method such as developed herein to assess the aerodynamic propagation losses through turbulent layers, it is recommended that further tests be conducted in which the experimental problems discussed above are eliminated. A more accurate evaluation of the mathematical prediction model can then be made.

REFERENCES

1. Tatarski, V. I., Wave Propagation in a Turbulent Medium, Dover, 1967.
2. Wolters, D. J., "Aerodynamic Effects on Airborne Optical Systems", McDonnell Aircraft Corp., MDC Report No. A2582, Dec. 1973.
3. Laufer, J., Private Communication.
4. Abramowitz, M. and Stegun, I. A., Handbook of Mathematical Functions, Dover, 1965.
5. Buell, D., "Aerodynamic Properties of a Flat Plate With Cavity for Optical-Propagation Studies", NASA TM-78487, June 1979.
6. Rose, W. C., Private Communication, 1977.
7. Bailey, W. H., Private Communication, 1977.

TABLE 1. SUMMARY OF GEOMETRICAL CONFIGURATIONS TESTED

	Clean plate	Turbulent boundary-layer thickener (V-K pins)	Boundary-layer fence A	Boundary-layer fence B	Boundary-layer fence C	Boundary-layer fence D	Boundary-layer fence E	Boundary-layer fence F	Boundary-layer fence G	Boundary-layer trip	Boundary-layer trip with V-K pins
Flat plate, cavity covered		1									
Flat plate, cavity open	8						13	11			
Flat plate, cavity open, porous cavity forward wall with mass injection	14										
Flat plate, cavity open, slotted cavity forward wall with mass injection											

FENCE DESCRIPTION

- A - 38% Porosity, MCAIR Design
- B - 58% Porosity, AFWL Design
- C - 2.3 cm height, slotted
- D - 2.3 cm height, 38% Porosity
- E - 2.3 cm height, 58% Porosity
- F - 4.6 cm height, 38% Porosity
- G - 4.6 cm height, 58% Porosity

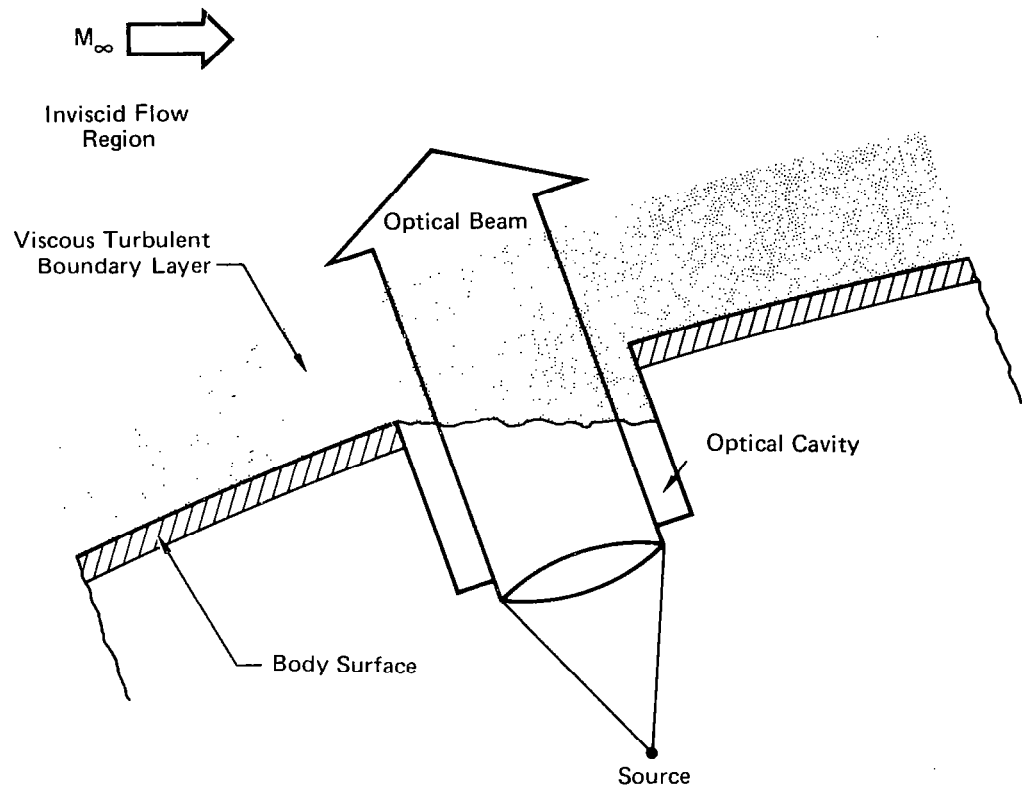


FIGURE 1
OPTICAL BEAM PROPAGATION THROUGH FLOW FIELD
SURROUNDING A MOVING BODY.

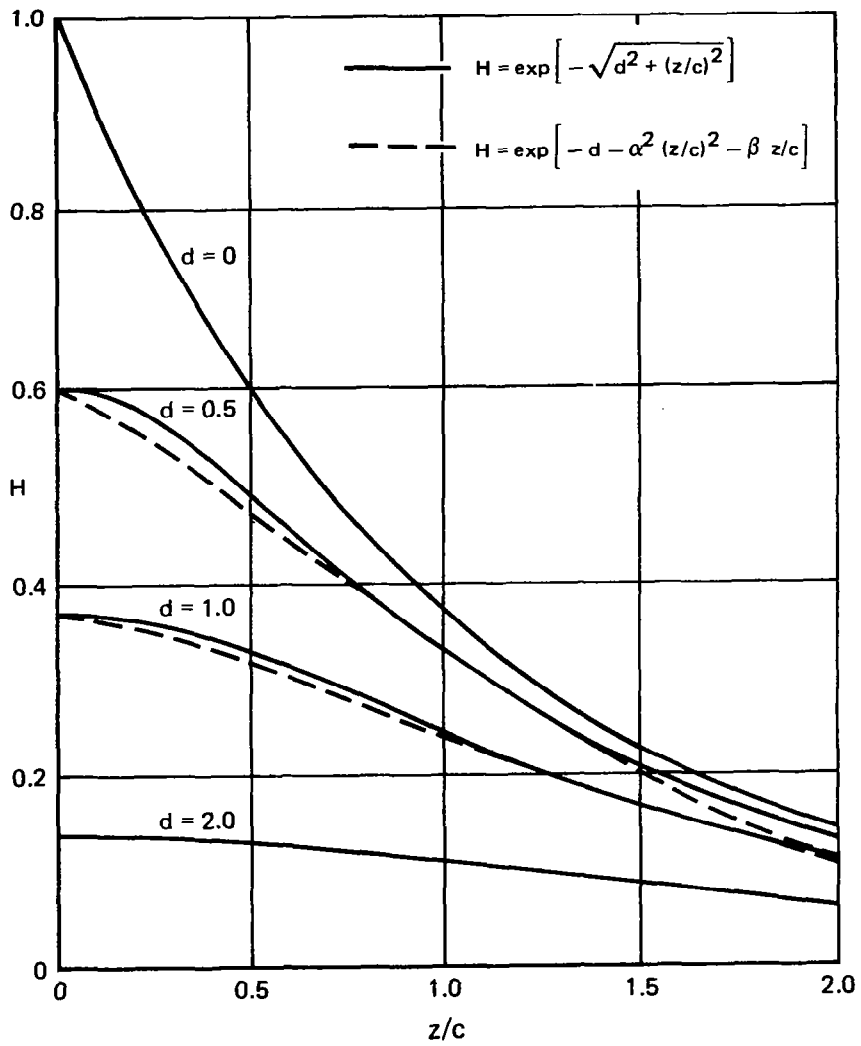


FIGURE 2
CORRELATION FUNCTION APPROXIMATION.

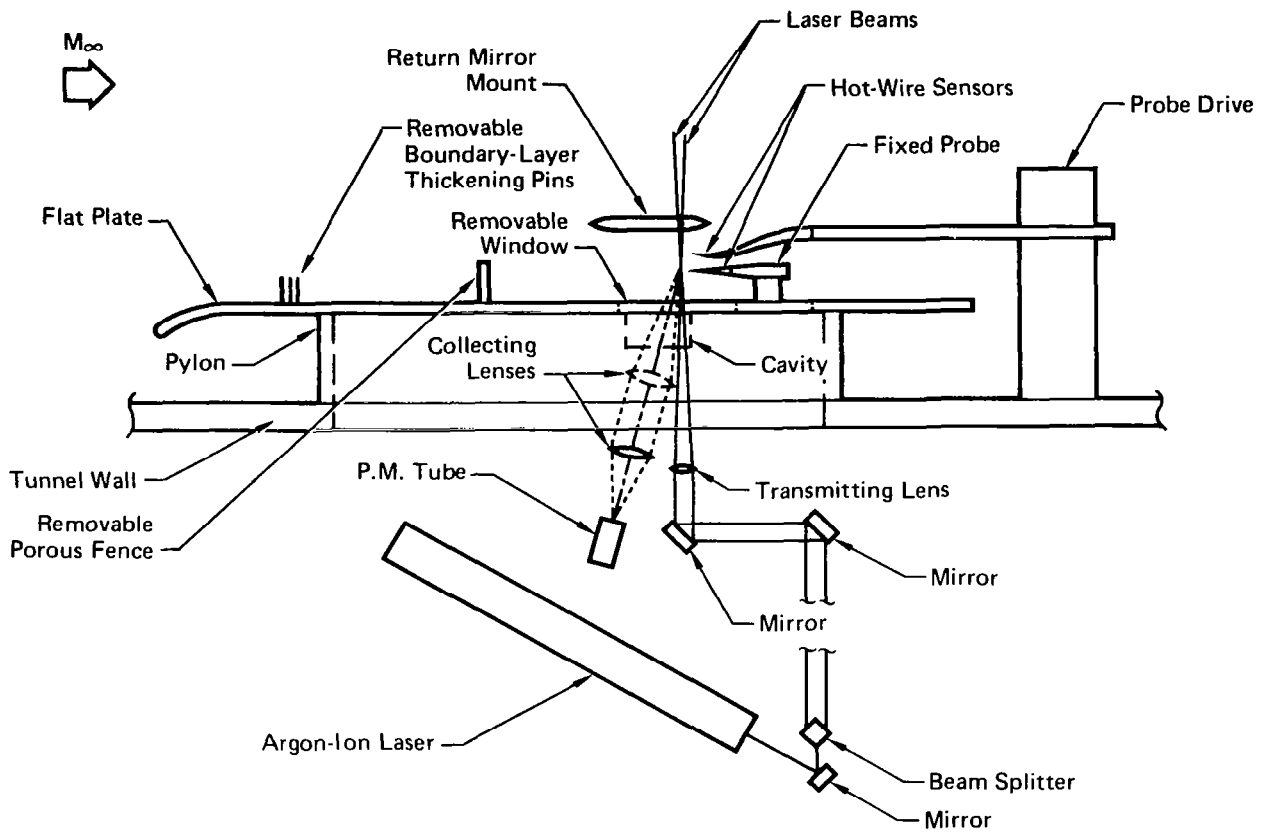
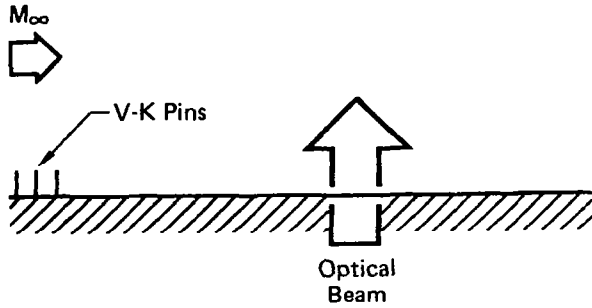


FIGURE 3
SCHEMATIC OF EXPERIMENTAL APPARATUS,
HOT-WIRE AND LDV SYSTEMS.

GP77-0692-23



	○	□
M_∞	= 0.6	0.9
Re	= 9.8×10^6	$9.8 \times 10^6/\text{meter}$
δ	= 10.8	11.2 cm
a	= 0.169	0.186
c	= 0.113	0.109
σ	= 0.0053	0.0073 kg/m ³

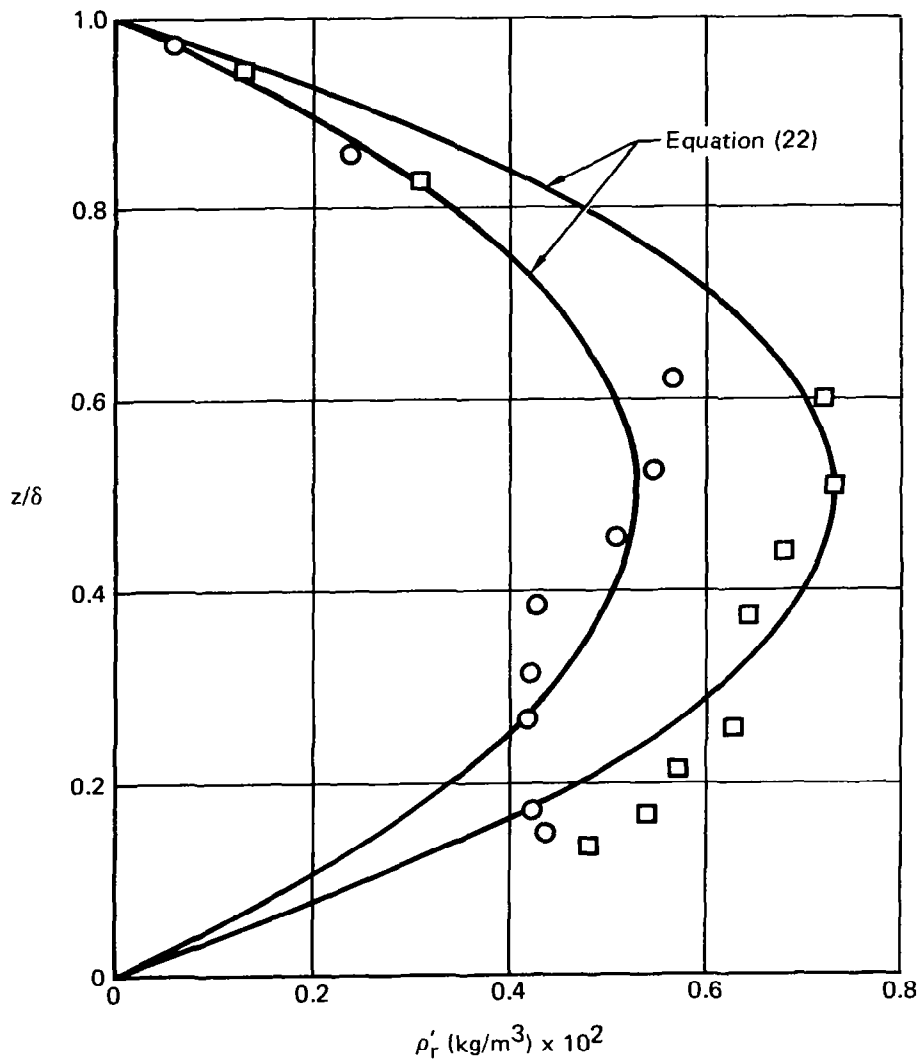


FIGURE 4
SUMMARY OF CONFIGURATION NO. 1 DATA.

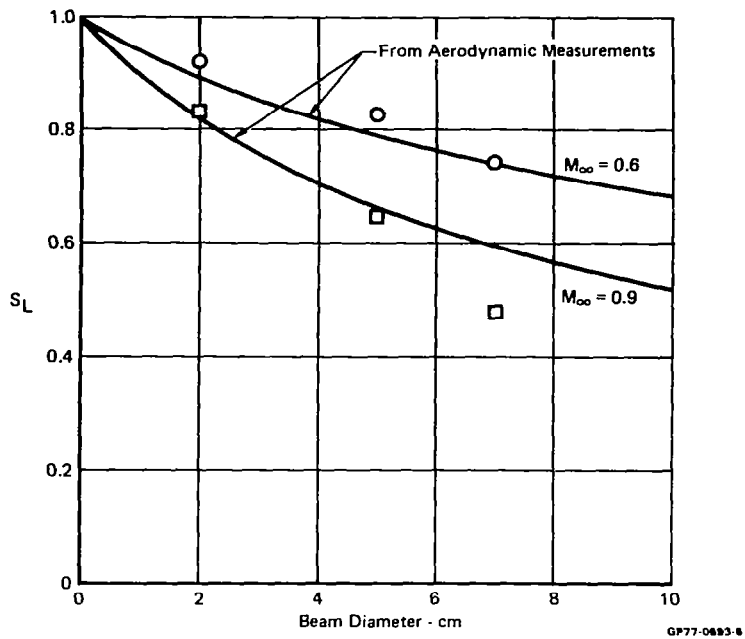


FIGURE 5
 LINE SPREAD STREHL RATIO.
 Configuration No. 1 - $Re = 9.8 \times 10^6$ /meter

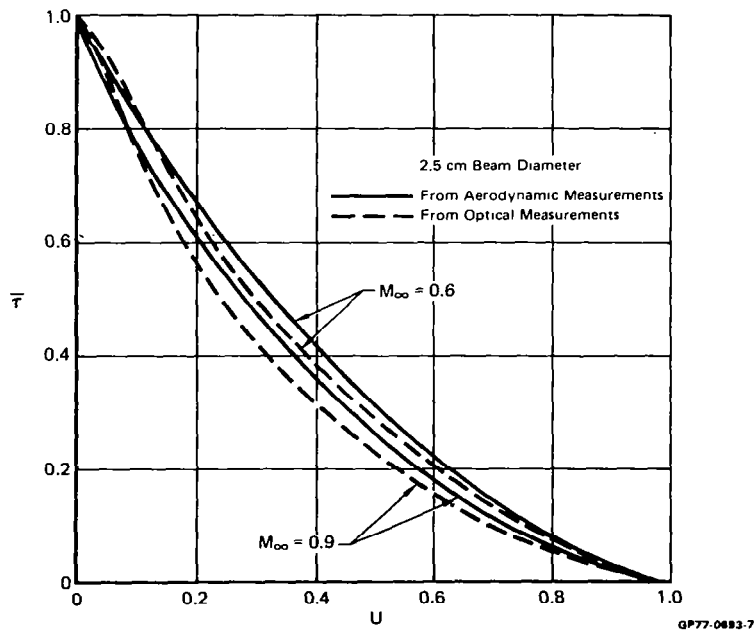
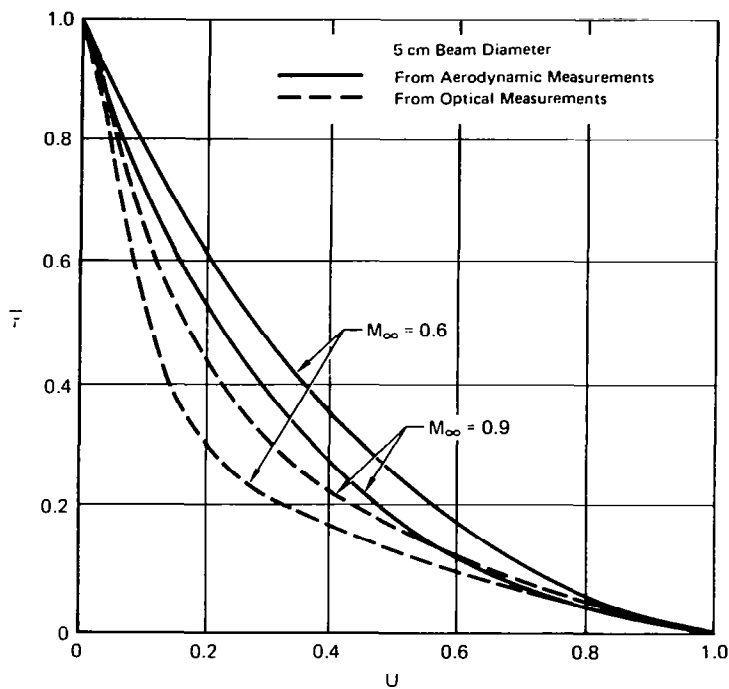
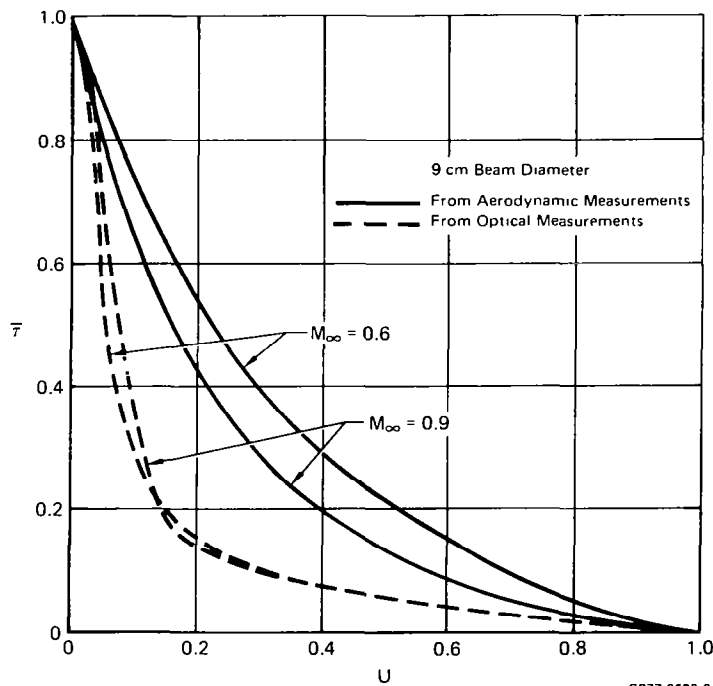


FIGURE 6
 MODULATION TRANSFER FUNCTION.
 Configuration No. 1 - $Re = 9.8 \times 10^6$ /meter



GP77-0693-8

FIGURE 7
MODULATION TRANSFER FUNCTION.
 Configuration No. 1 - $Re = 9.8 \times 10^6$ /meter



GP77-0693-9

FIGURE 8
MODULATION TRANSFER FUNCTION.
 Configuration No. 1 - $Re = 9.8 \times 10^6$ /meter

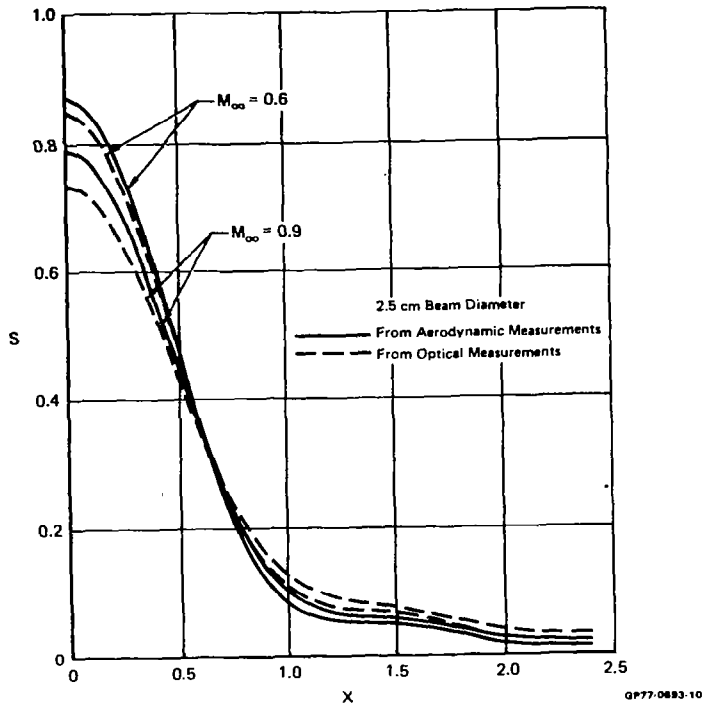


FIGURE 9
 LINE SPREAD FUNCTION.
 Configuration No. 1 - $Re = 9.8 \times 10^6$ /meter

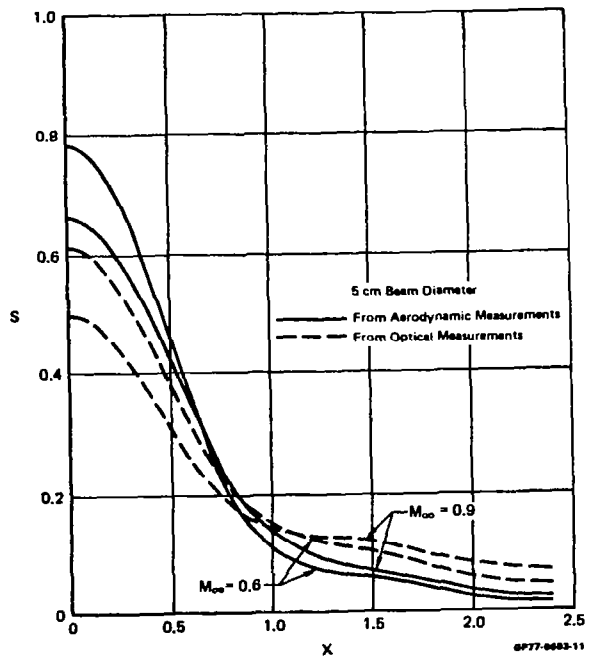


FIGURE 10
 LINE SPREAD FUNCTION.
 Configuration No. 1 - $Re = 9.8 \times 10^6$ /meter

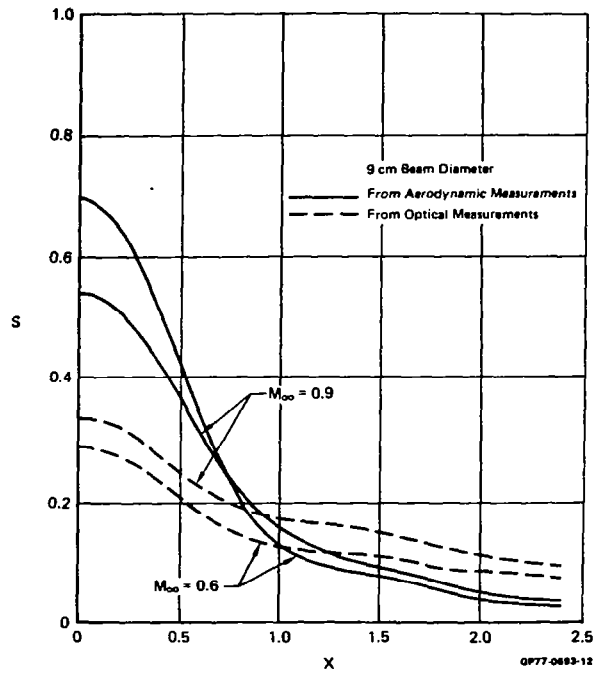
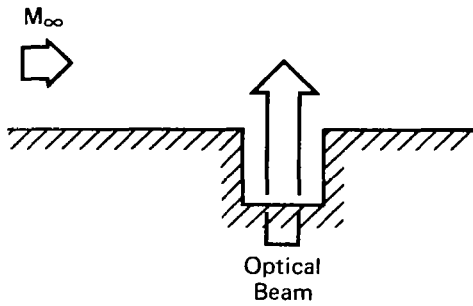
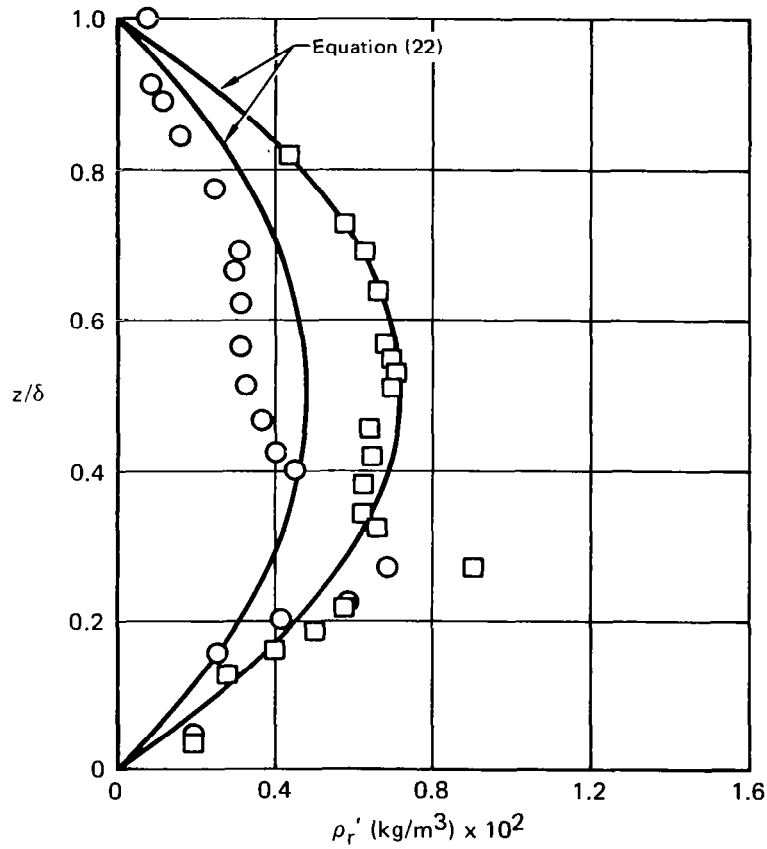


FIGURE 11
 LINE SPREAD FUNCTION.
 Configuration No. 1 - $Re = 9.8 \times 10^6$ /meter



○	□
$M_\infty = 0.6$	0.9
$Re = 9.8 \times 10^6$	$9.8 \times 10^6/\text{meter}$
$\delta = 11.4$	14.0 cm
$a = 0.222$	0.218
$c = 0.073$	0.118
$\sigma = 0.0048$	0.0072 kg/m^3



GP77-0893-27

FIGURE 12
SUMMARY OF CONFIGURATION NO. 8 DATA.

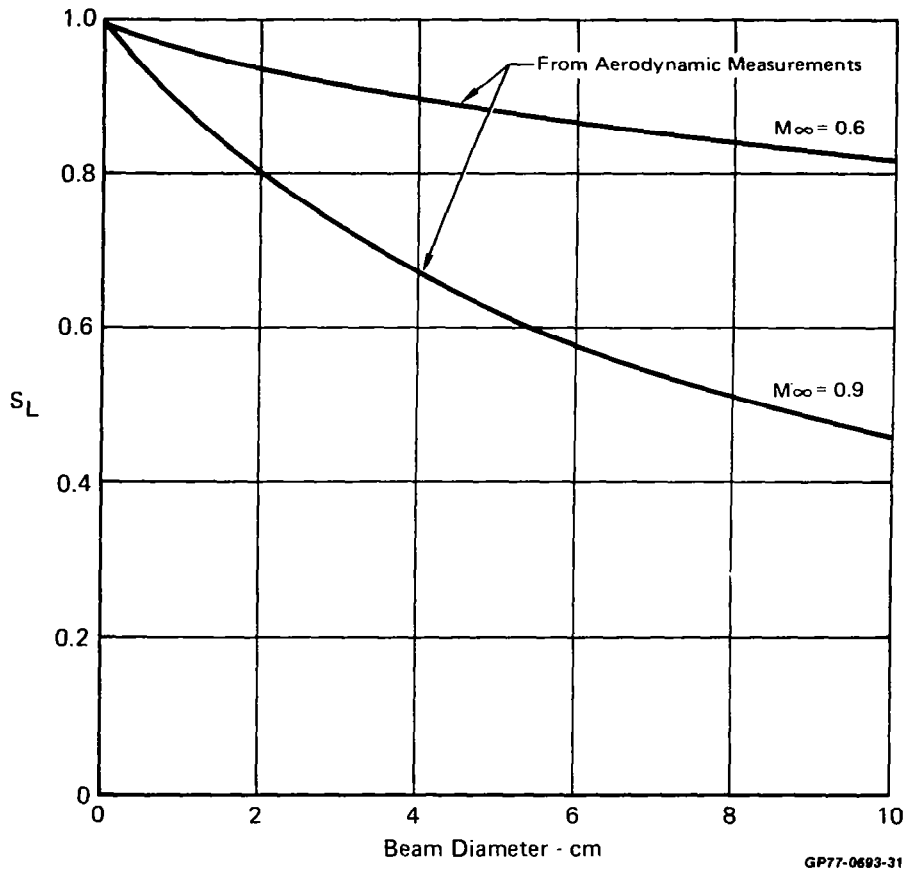


FIGURE 13
 LINE SPREAD STREHL RATIO.
 Configuration No. 8 - $Re = 9.8 \times 10^6$ /meter

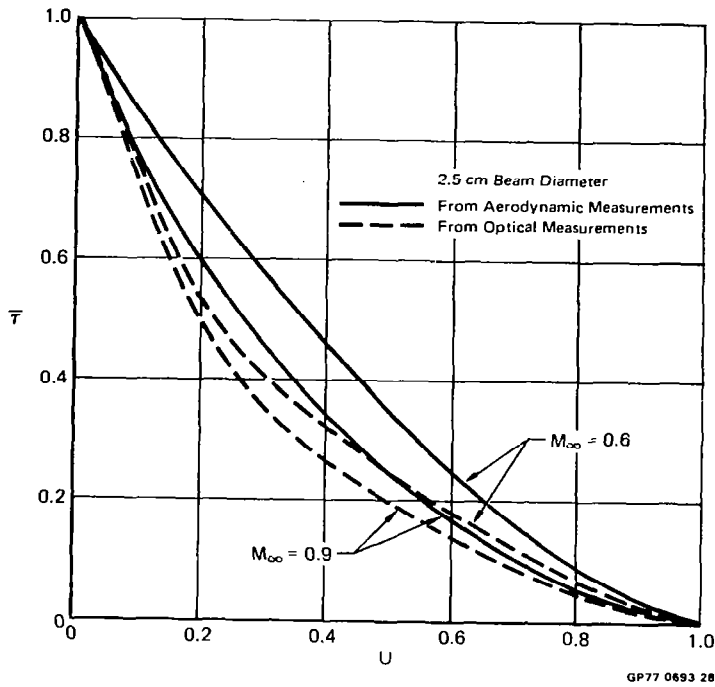


FIGURE 14
 MODULATION TRANSFER FUNCTION.
 Configuration No. 8 - $Re = 9.8 \times 10^6$ /meter

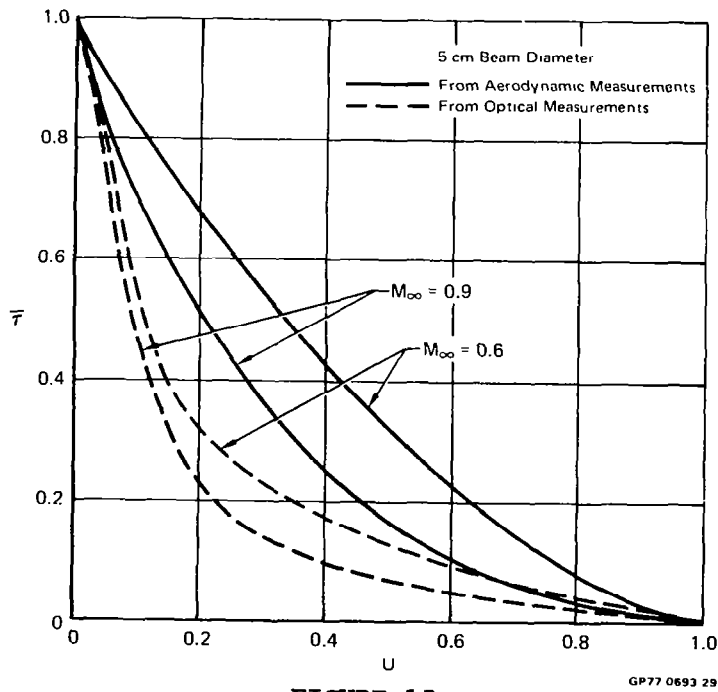
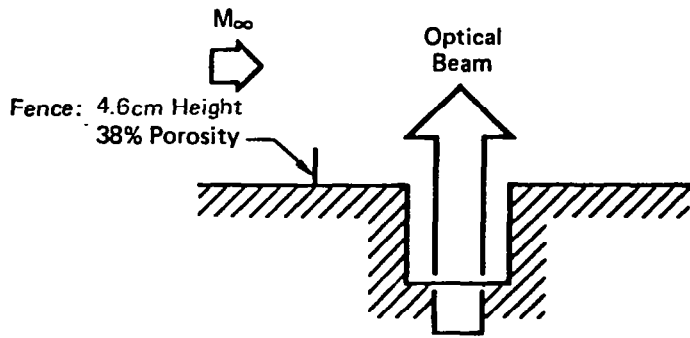


FIGURE 15
 MODULATION TRANSFER FUNCTION.
 Configuration No. 8 - $Re = 9.8 \times 10^6$ /meter



○	□
$M_\infty = 0.6$	0.9
$Re = 9.8 \times 10^6$	$9.8 \times 10^6/\text{meter}$
$\delta = 8.9$	10.2 cm
$a = 0.211$	0.212
$c = 0.149$	0.118
$\sigma = 0.0060$	0.0100 kg/m^3

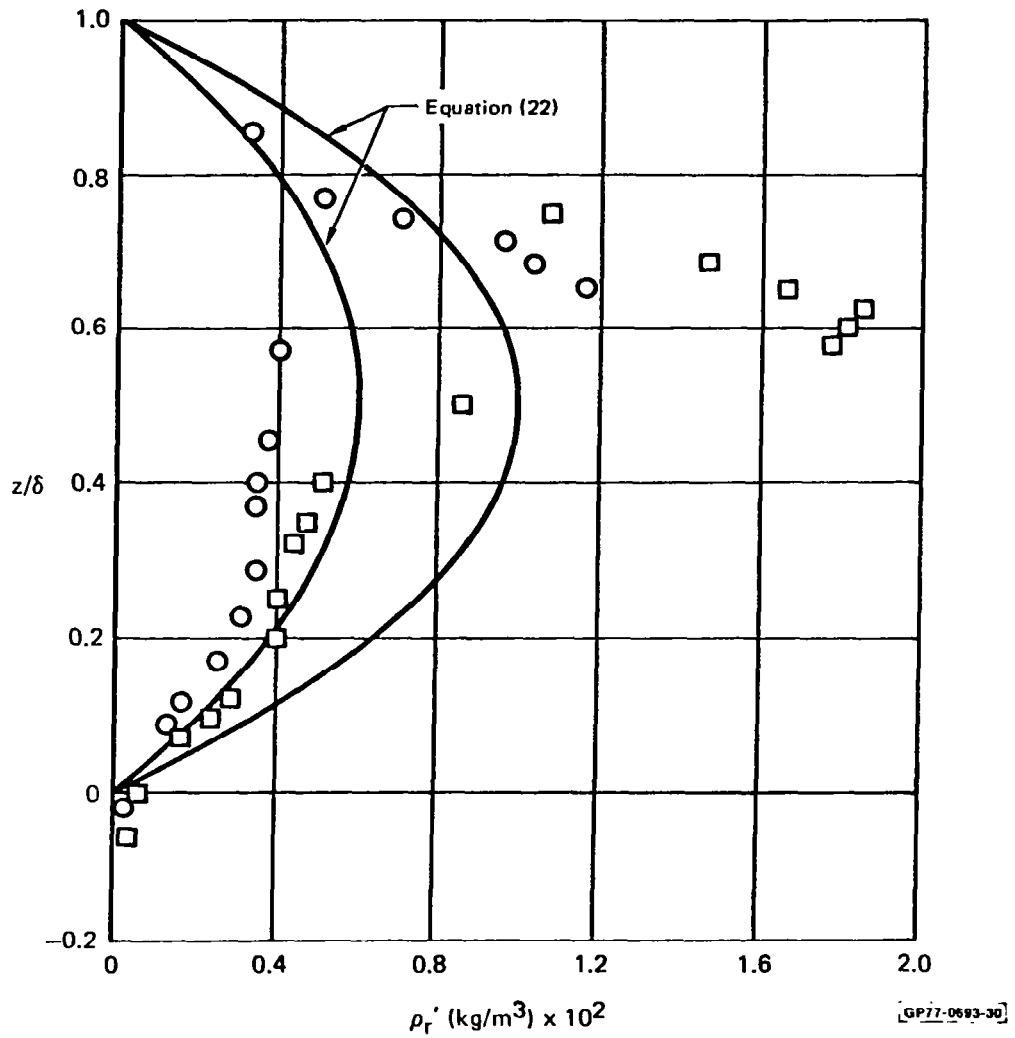
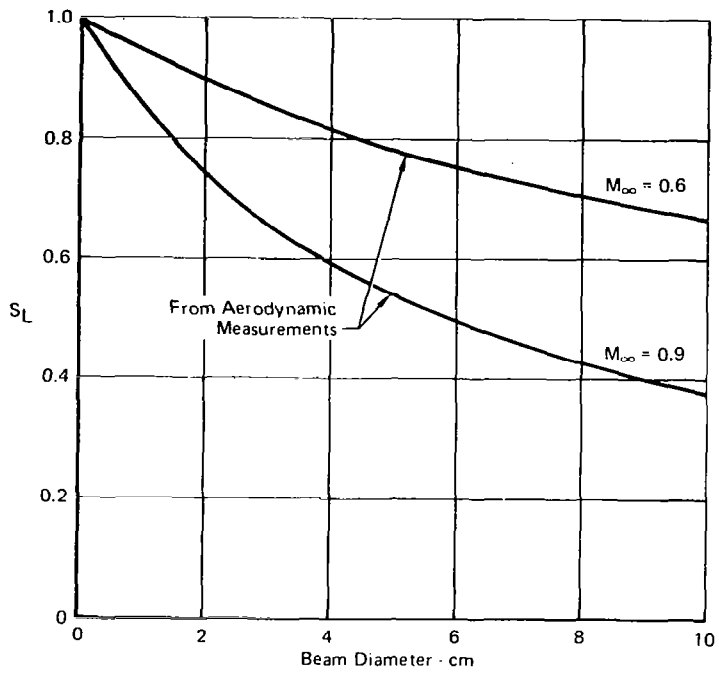


FIGURE 16
SUMMARY OF CONFIGURATION NO. 11 DATA.



GP77 0893 26

FIGURE 17
LINE SPREAD STREHL RATIO.
 Configuration No. 11 - $Re = 9.8 \times 10^6$ /meter

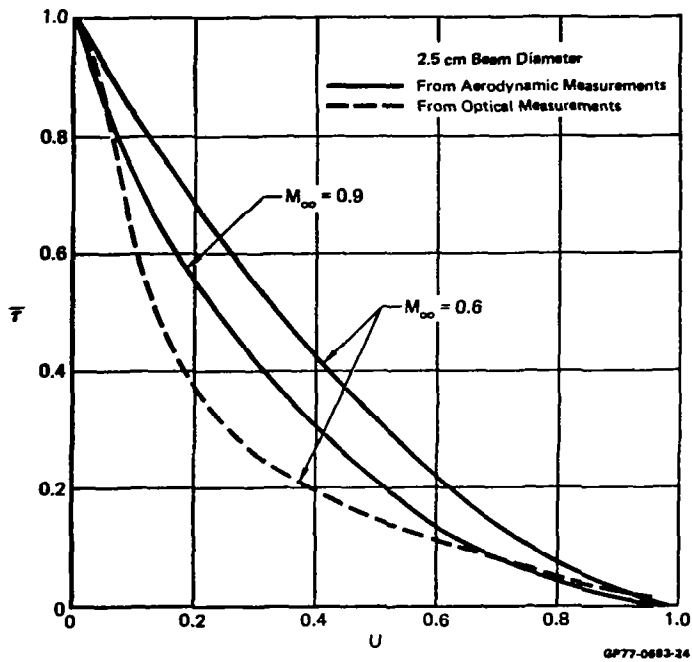


FIGURE 18
 MODULATION TRANSFER FUNCTION.
 Configuration No. 11 - $Re = 9.8 \times 10^6$ /meter

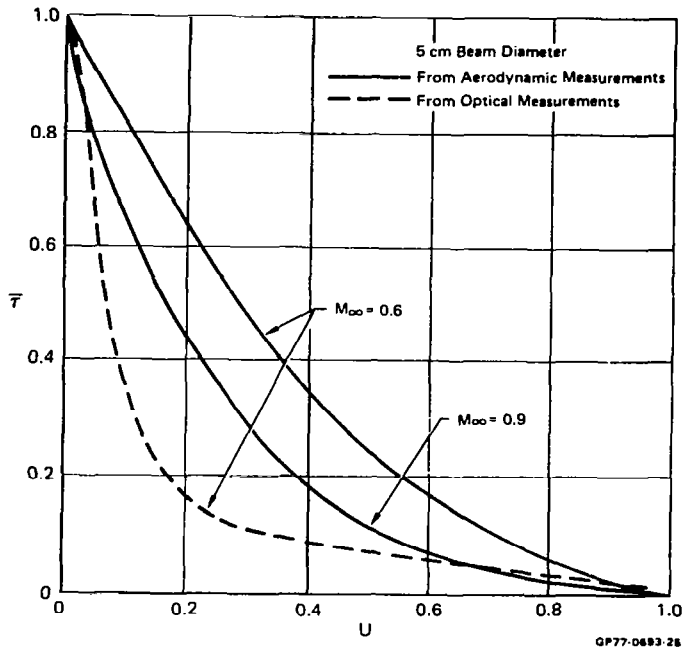
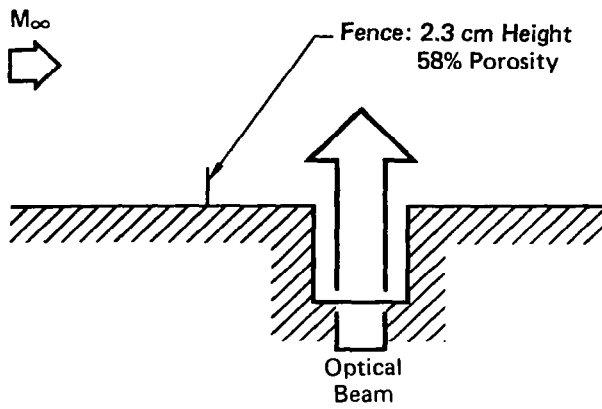


FIGURE 19
 MODULATION TRANSFER FUNCTION.
 Configuration No. 11 - $Re = 9.8 \times 10^6$ /meter



○	□
$M_\infty = 0.6$	0.9
$Re = 9.8 \times 10^6$	$9.8 \times 10^6/\text{meter}$
$\delta = 10.2$	11.4 cm
$a = 0.173$	0.262
$c = 0.050$	0.089
$\sigma = 0.0060$	0.0129 kg/m^3

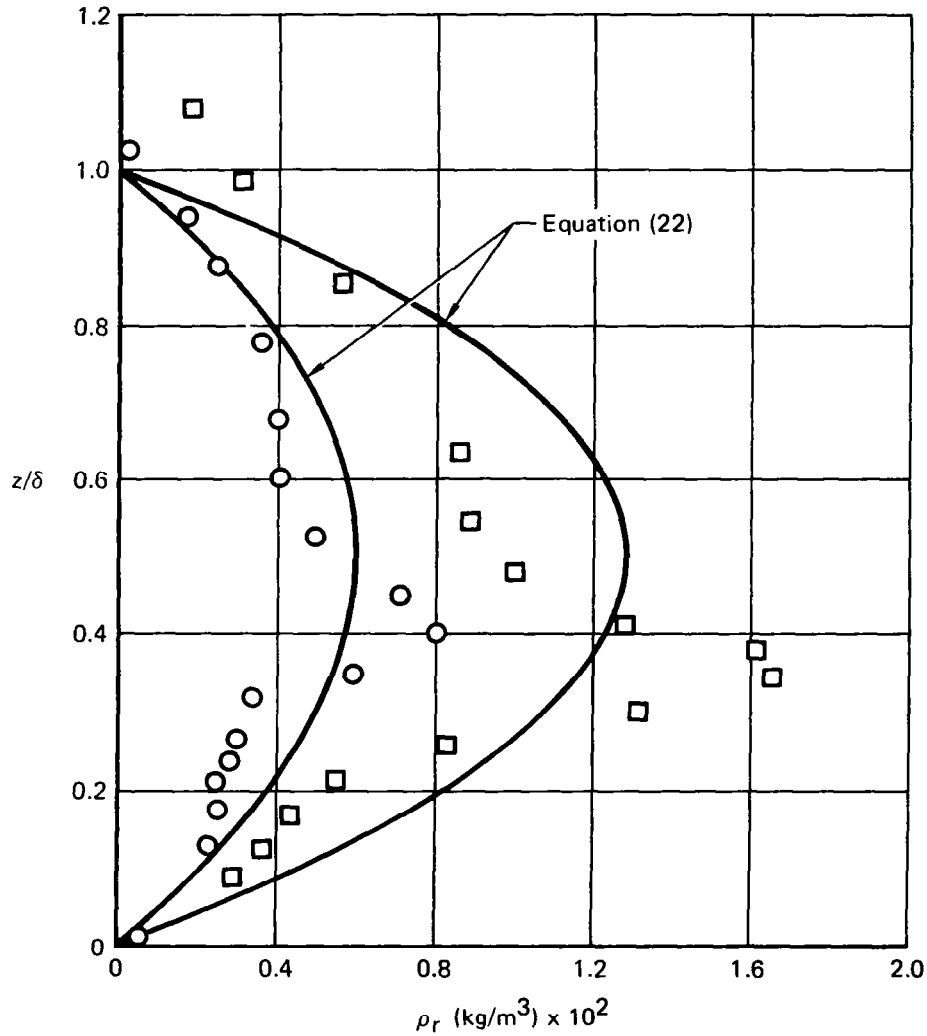


FIGURE 20
SUMMARY OF CONFIGURATION NO. 13 DATA.

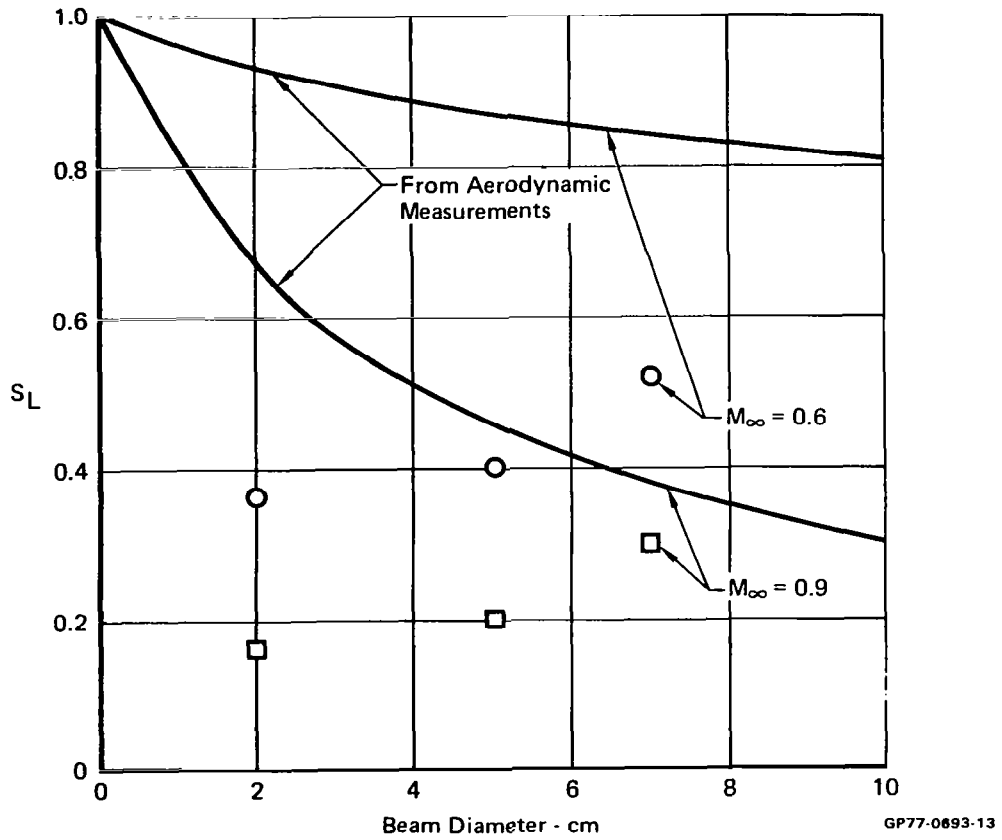


FIGURE 21
 LINE SPREAD STREHL RATIO.
 Configuration No. 13 - $Re = 9.8 \times 10^6$ /meter

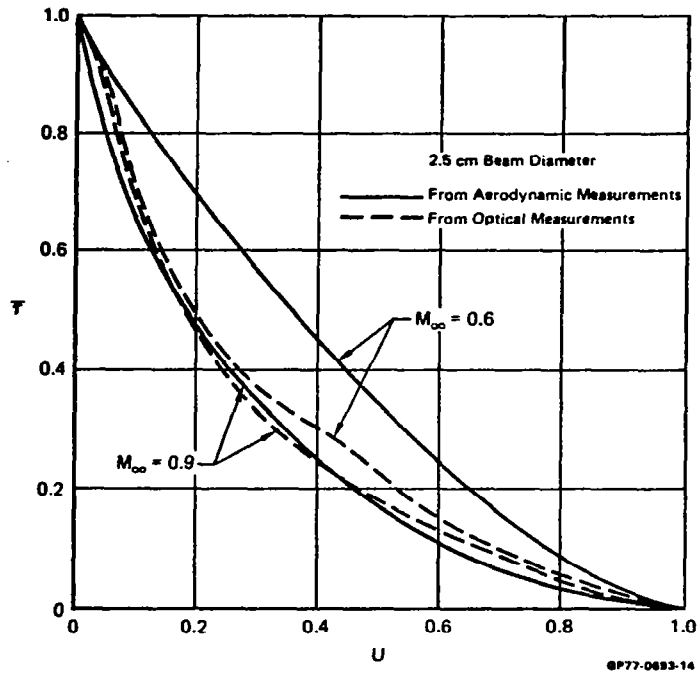


FIGURE 22
 MODULATION TRANSFER FUNCTION.
 Configuration No. 13 - $Re = 9.8 \times 10^6$ /meter

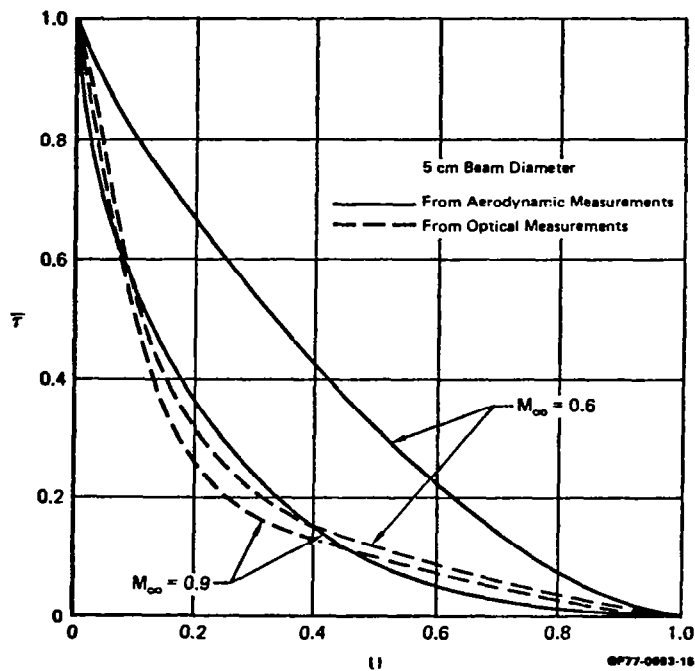


FIGURE 23
 MODULATION TRANSFER FUNCTION.
 Configuration No. 13 - $Re = 9.8 \times 10^6$ /meter

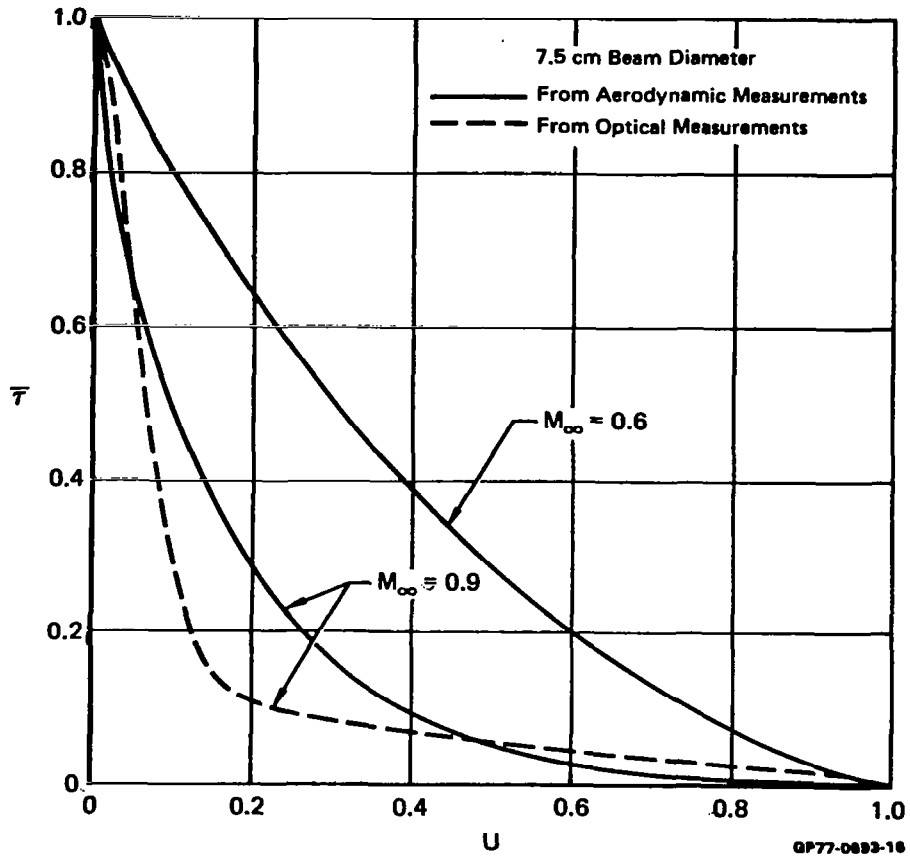
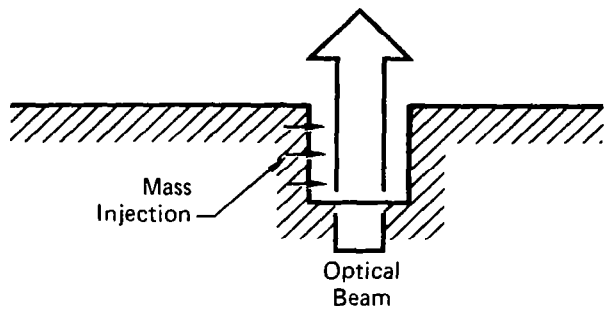
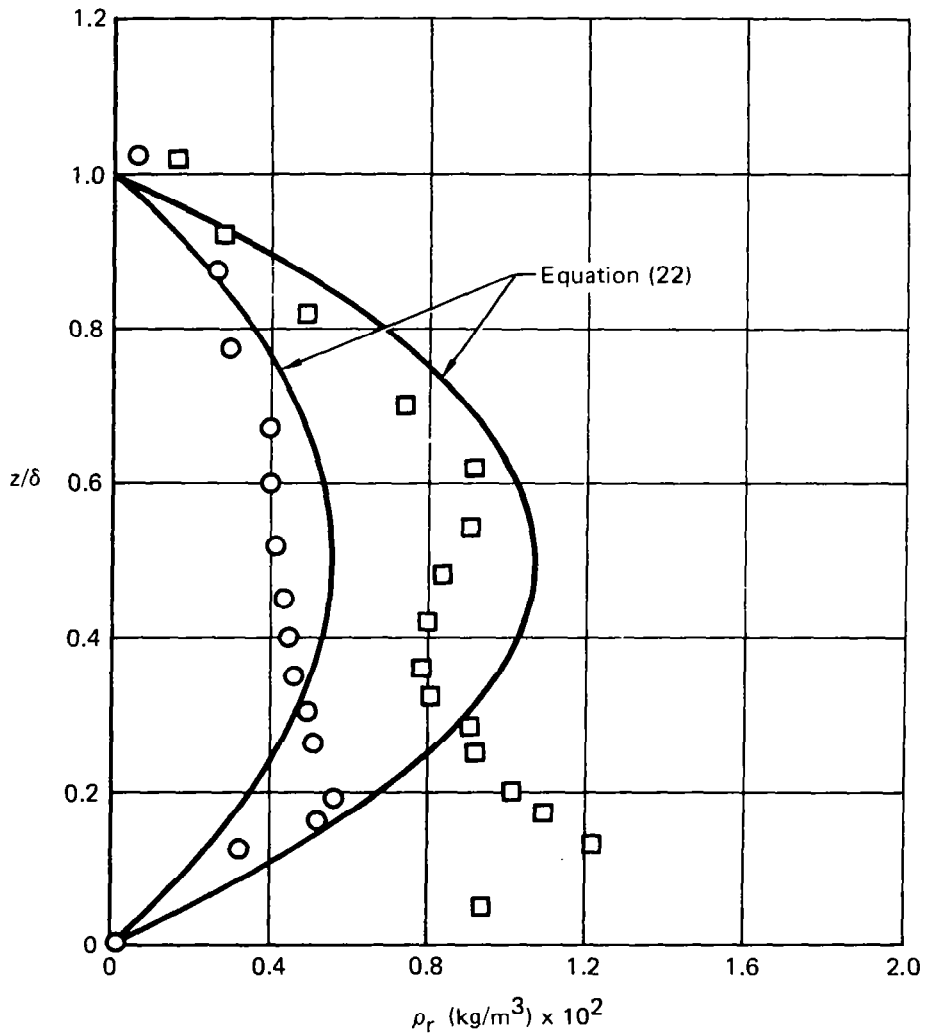


FIGURE 24
 MODULATION TRANSFER FUNCTION.
 Configuration No. 13 - $Re = 9.8 \times 10^6$ /meter

M_∞

	○	□
M_∞	= 0.6	0.9
Re	= 9.8×10^6	$9.8 \times 10^6/\text{meter}$
δ	= 10.2	12.7 cm
a	= 0.238	0.328
c	= 0.088	0.104
σ	= 0.0057	0.0107 kg/m ³
\dot{m}	= 0	0 kg/sec



GP77-0693.4

FIGURE 25
 SUMMARY OF CONFIGURATION NO. 14 DATA.

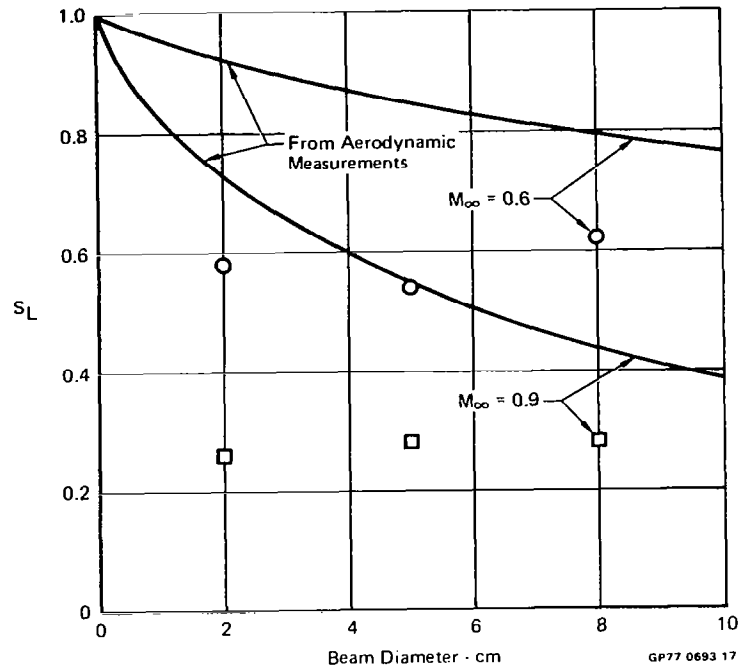


FIGURE 26
 LINE SPREAD STREHL RATIO.
 Configuration No. 14 - $\dot{m} = 0$; $Re = 9.8 \times 10^6$ /meter

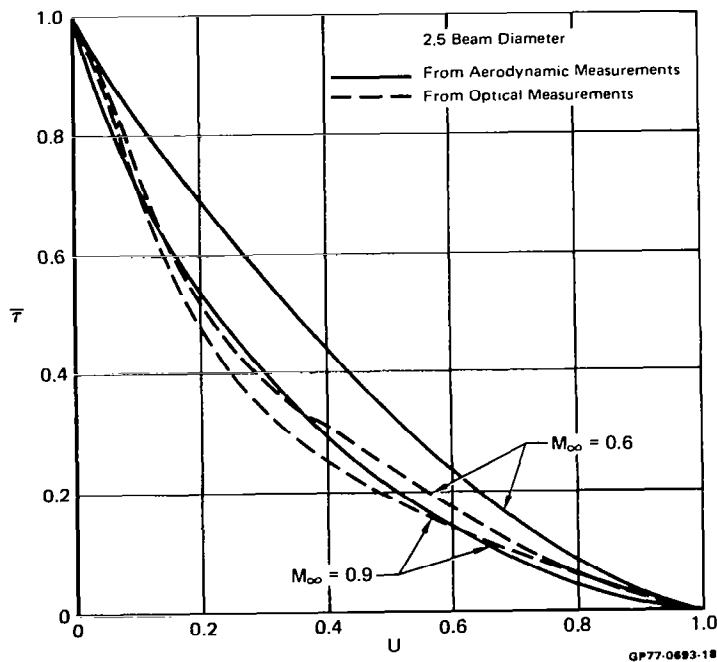


FIGURE 27
 MODULATION TRANSFER FUNCTION.
 Configuration No. 14 - $\dot{m} = 0$; $Re = 9.8 \times 10^6$ /meter

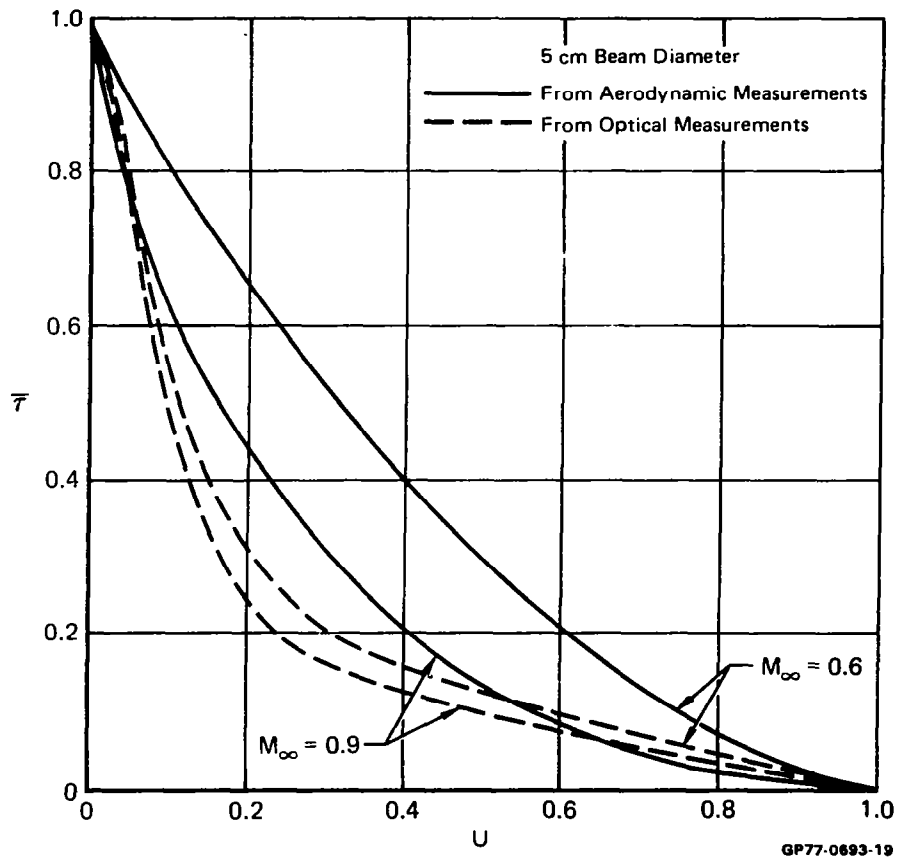
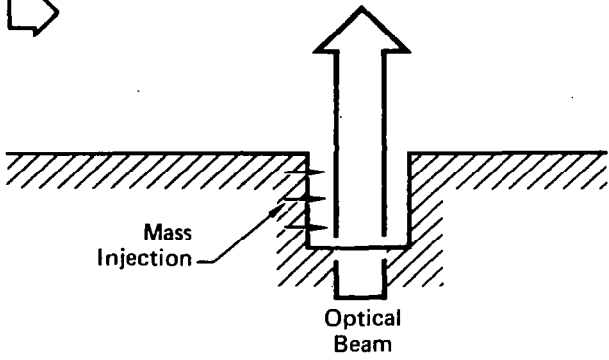
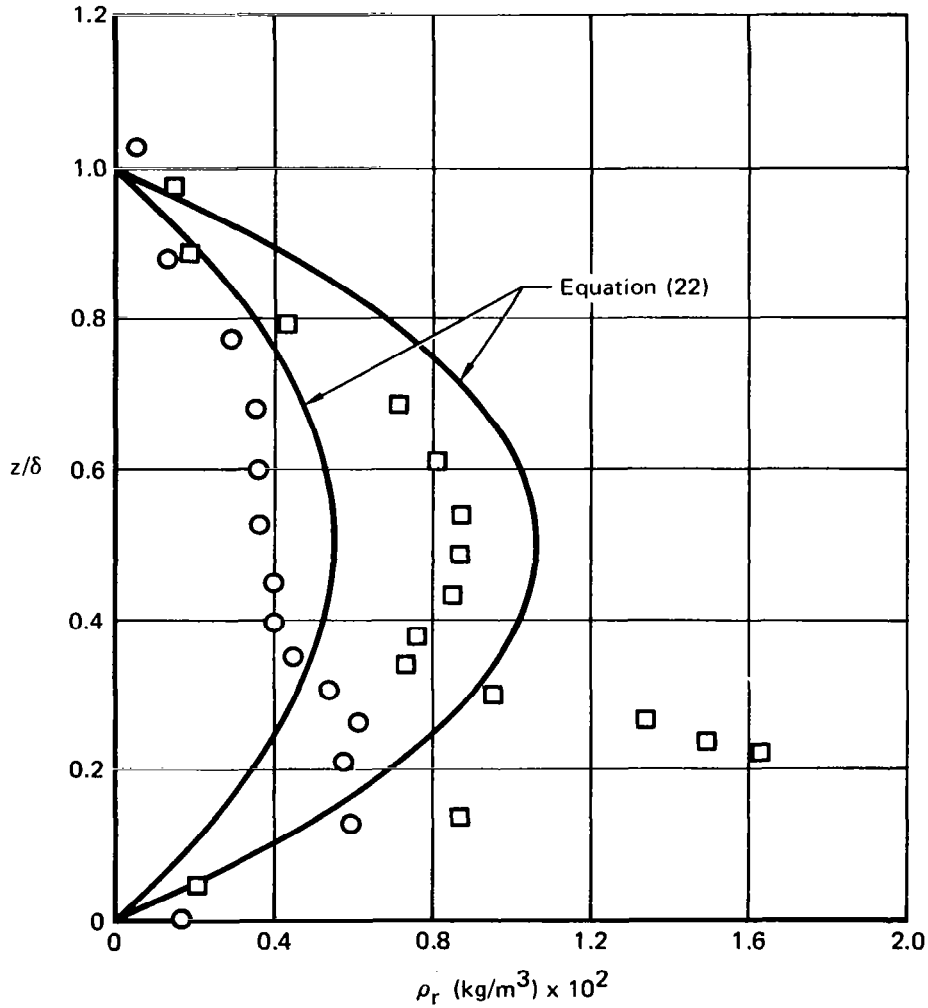


FIGURE 28
 MODULATION TRANSFER FUNCTION.
 Configuration No. 14 - $\dot{m} = 0$; $Re = 9.8 \times 10^6$ /meter

M_∞

	○	□
M_∞	= 0.6	0.9
Re	= 9.8×10^6	$9.8 \times 10^6/\text{meter}$
δ	= 10.2	13.4 cm
a	= .200	0.395
c	= 0.051	0.084
σ	= 0.0055	0.0105 kg/m ³
\dot{m}	= 0.25	0.25 kg/sec



GP77-0693-5

FIGURE 29
 SUMMARY OF CONFIGURATION NO. 14 DATA.

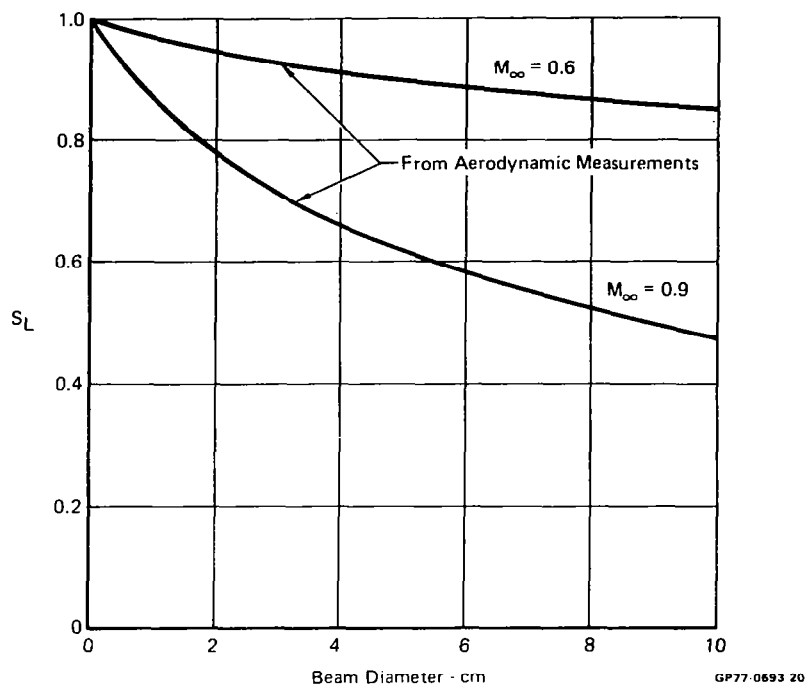


FIGURE 30
LINE SPREAD STREHL RATIO.
 Configuration No. 14 - $\dot{m} = 0.25$; $Re = 9.8 \times 10^6$ /meter

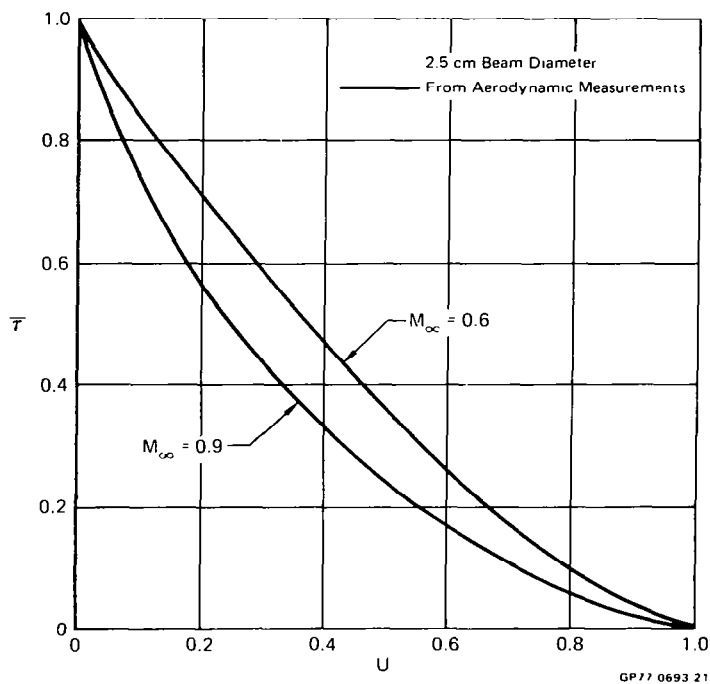


FIGURE 31
MODULATION TRANSFER FUNCTION.
 Configuration No. 14 - $\dot{m} = 0.25$; $Re = 9.8 \times 10^6$ /meter

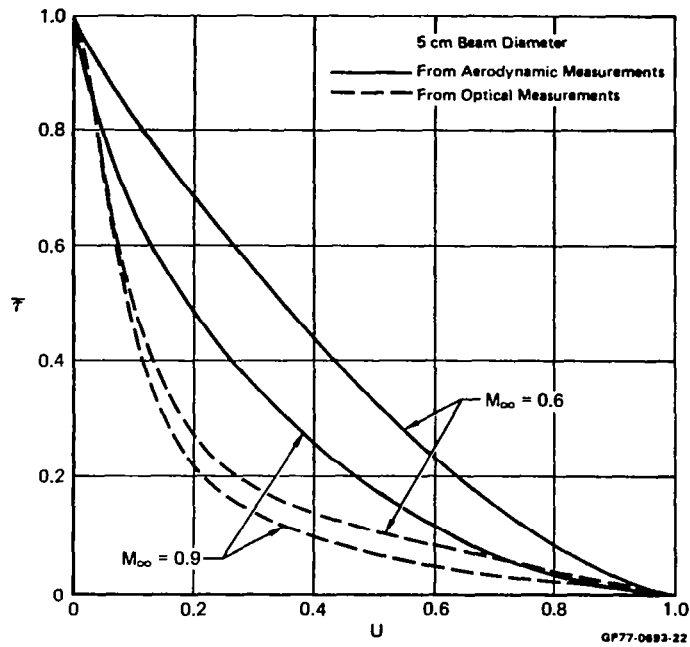


FIGURE 32
 MODULATION TRANSFER FUNCTION.
 Configuration No. 14 - $\dot{m} = 0.25$; $Re = 9.8 \times 10^6$ /meter